University of Southern Denmark
Mads Clausen Institute

Templates for integrated nanofiber growth

Ph.D. thesis

Roana Melina de Oliveira Hansen

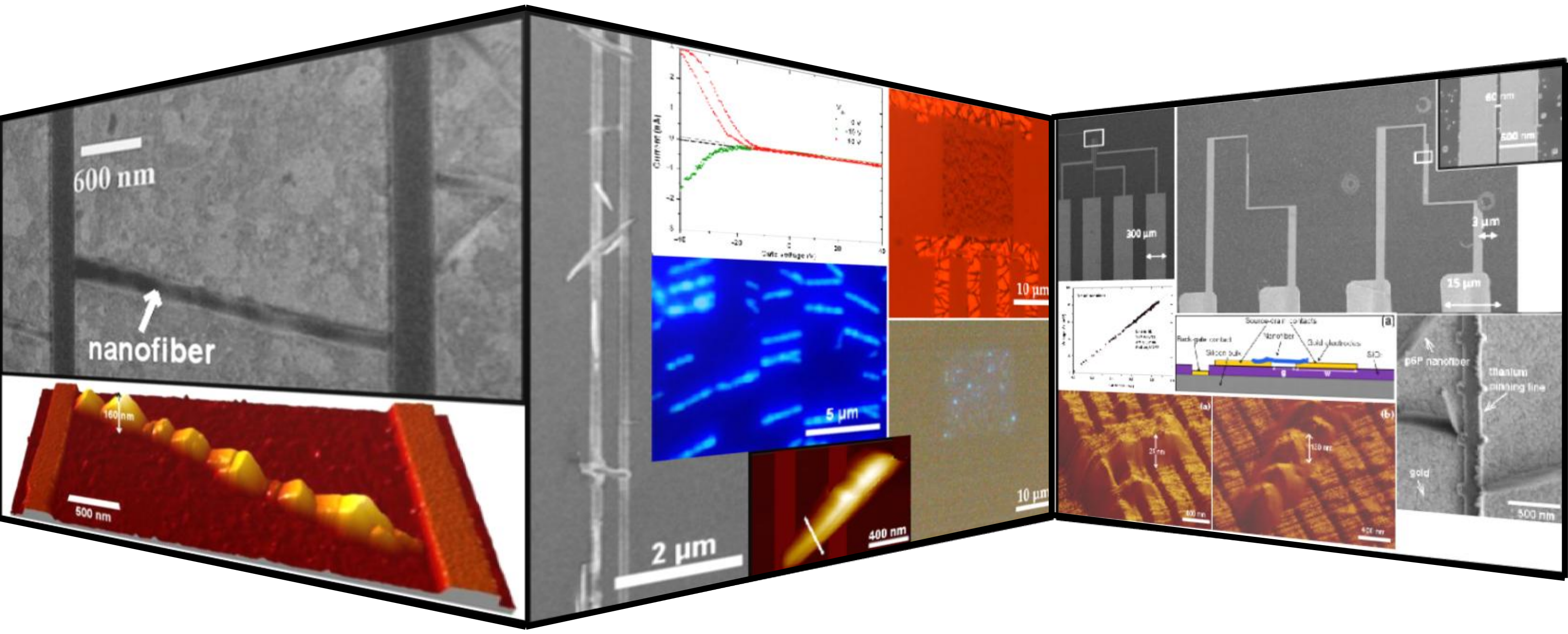

RESUMÉ

Para-hexaphenylene (p6P) molekyler har evnen til selv at samle sig til organiske nanofibre. Disse nanofibre har unikke optoelektroniske egenskaber, hvilket gør dem interessante at bruge som elementer i elektroniske og optoelektroniske apparater. Typisk, bliver disse nanofibre dyrket på et specifikt enkelt-krystallinsk substrat, såsom muscovite mica, hvorpå lange, gensidige parallelle nanofibre selv-samles, under pådampning af det organiske materiale ved de høje vakuum forhold. Dog er den manglende evne til yderligere at behandle disse substrater, og integrere sådanne skrøbelige nanostrukturer med de nødvendige grænseflade kredsløb, (såsom metal elektroder til elektriske forbindelser), fortsat en væsentlig hindring for omfattende implementering. Udviklingen i brugen af in-situ, udgør en meget lovende strategi for integration af funktionelle nanostrukturer i apparaters opbygning, på grund af muligheden for mange parallelle integrationer. Udover sådanne single-krystallinske skabeloner, kan nanofibre også dyrkes på ikke-krystallinske guld overflader, hvorpå orienteringen af nanofibre kan manipuleres ved at strukturere guld overfladen forud for p6P depositionen.

I dette projekt, vil en ny metode til in-situ vækst i p6P nanofibre på nano-strukturerede guld overflader blive præsenteret. Substratet forberedes af traditionelle nanofabrikationsteknikker såsom e-beam litografi og metal deposition, som øger substratets potentiale som platform for enheder i apparater. Nogle af de resultater, som præsenteres her viser, at både vækst retning og nanofibrenes længde og placering kan kontrolleres ved placering af nano-strukturerede linjer på substratet. Disse linjer kan bruges til at guide overfladens spredning af molekyler, og dermed styre selvsamlings processen for de organiske molekyler, hvilket fører til morfologisk veldefinerede molekylære nanofibers med foretrukne vækst retninger. Det er blevet vist, at den foretrukne vækst retning på nanofibre er vinkelret til disse strukturer, mens deres længdeskalaer er begrænset af størrelsen og placeringen af strukturerne. Dette arbejde er derfor udtryk for en ny teknik, som kan være nyttige i fremtidige organiske nanofiber baserede applikationer.

Vi har også demonstreret, hvordan guld rister som er fabrikeret på et isolerende substrat kan skabe elektrisk kontakt til in-situ dyrket p6P nanofibre. I en videreudvikling af denne metode, er de organiske in-situ rettede nanostrukturere dyrket mellem præfabrikerede kontakter, som er source-drain guld elektroder på en transistor platform (indeholdende bottom- eller top-gate) på silicium dioxid mønstrede ved en kombination af optiske litografi og e-

beam litografi. Størrelsen af guld elektroderne har stor indflydelse på morfologien på de endelige strukturer, hvilket bl.a. fører til forskellige elektriske egenskaber. Transistorens design påvirke dens egenskaber, og top-gate konfigurationen har vist sig at have en stærkere gate effekt. Desuden blev LED enheder fabrikeret, hvilket viste sig i form af nanofibre der udsendte lys, når en AC-spænding blev tilført gaten.

Platforme til 4-punkts målinger blev konstrueret for at fjerne kontakt modstanden og fastslå nanofibrenes modstand. Evnen til at opnå in-situ vækst af p6P nanostrukturer på enhedsplatforme åbner en bred vifte af mulige anvendelser, herunder fremstilling af organiske lysdioder og andre optoelektroniske anordninger.

ABSTRACT

Para-hexaphenylene (p6P) molecules have the ability to self-assemble into organic nanofibers. These nanofibers hold unique optoelectronic properties, which make them interesting candidates as elements in electronic and optoelectronic devices. Typically these nanofibers are grown on specific single-crystalline substrates, such as muscovite mica, on which long, mutually parallel nanofibers are self-assembled upon vapor deposition of the organic material under high vacuum conditions. However, the lack of ability to further process these substrates and for integration of such fragile nanostructures with the necessary interface circuitry such as metal electrodes for electrical connection continues to be a significant hindrance toward their large-scale implementation. In-situ growth constitutes a very promising strategy for integrating functional nanostructures into device platforms due to the possibility of parallel, high-volume integration. Besides such single-crystalline templates, the nanofibers can also be grown on non-crystalline gold surfaces, on which the orientation of the nanofibers can be manipulated by structuring the gold surface prior to p6P deposition.

In this work, a novel method for in-situ growth of p6P nanofibers on nano-structured gold surfaces is presented. The substrates are prepared by conventional nanofabrication techniques such as e-beam lithography and metal deposition, which increase their potential as device platforms. Some of the results presented here demonstrate, that both the growth direction and the nanofiber length and position can be controlled by placement of nano-structured lines on the substrate. These lines can be used to guide the surface diffusion and thereby steer the self-assembly process of the organic molecules leading to morphologically well-defined molecular nanofibers with preferred growth directions. It is shown that the preferred growth direction of the nanofibers is perpendicular to these structures whereas their length scales are limited by the size and placement of the structures. This work therefore demonstrates a new technique, which can be useful within future organic nanofiber based applications. We also demonstrated how gold gratings fabricated on an insulating substrate can enable electrical contact to in-situ grown p6P nanofibers.

In a further development of this method, in-situ directed growth of such organic nanostructures were performed between pre-fabricated contacts, which are source–drain gold electrodes on a transistor platform (containing bottom- or top-gate) on silicon dioxide. The substrates were patterned by a

combination of optical lithography and electron beam lithography. The dimensions of the gold electrodes strongly influence the morphology of the resulting structures leading to notably different electrical properties. The transistor design influences its electrical characteristics, and the top-gate configuration shows to have the stronger gate effect. In addition, platforms for light-emitting devices were fabricated, and the nanofibers did emit light when an AC voltage was applied to the gate. Platforms for 4-point measurements were fabricated to eliminate contact resistances and determine the nanofibers intrinsic resistance and resistivity.

The large-scale fabrication of such small device platforms was demonstrated by using nano-imprint lithography (NIL).

The ability to achieve in-situ growth of p6P nanostructures on device platforms opens a wide range of possible applications including fabrication of organic LEDs and other optoelectronic devices.

PREFACE

This thesis is part of the requirements for achieving the Ph.D. degree at the University of Southern Denmark (SDU). This work has been carried out at the Mads Clausen Institute at SDU in Sønderborg, at the NanoSYD group. The project supervisors are Professor Horst-Günter Rubahn and Associate Professor Jakob Kjelstrup-Hansen. Several publications were made during this project, and they are listed on the thesis end.

This work was financially supported by the Danish Council for Technology and Innovation through the Octopus innovation consortium.

I would like to acknowledge several people for their support during this project, especially Jakob Kjelstrup-Hansen and Horst-Günter Rubahn, my supervisors, for the help in many different aspects. Many other members of NanoSYD should be acknowledged, including Morten Madsen, Luciana Tavares, Xuhai Liu, Kasper Thilsing-Hansen and all my colleagues, for their kindness and helpful support. Also, I would like to thanks Henrik Hartmann Henrichsen for the LabVIEW programs and Rasmus Haugstrup Pedersen and Nikolaj Gadegaard for the help during my environmental change at University of Glasgow.

In addition, I would like to thank my husband Jesper, for his constant support and comprehension during this project.

TABLE OF CONTENTS

GLOSSARY

AFM: Atomic Force Microscopy

AR-ULP: Underlayer lift-off polymer for NanoImprint Lithography

AR- UVM: QuickMold™ polymer for NanoImprint Stamps

AR-UVP: UV sensitive polymer for NanoImprint

DTI: Danish Technological Institute

DTU: Technical University of Denmark

EBL: Electron Beam Lithography

GaAs: Galium Arsenide

HF: Hydrofluoric Acid

HOMO: Highest Occupied Molecular Orbital

ICP-RIE: Inductively Coupled Plasma- Reactive Ion Etching

IPA: Isopropyl Alcohol

ITO: Indium Tin Oxide

KCl: Potassium Chloride

LEDs: Light Emitting Diodes

LUMO: Lowest Unoccupied Molecular Orbital

MIBK: Methyl Isobutyl Ketone

NIL: NanoImprint Lithography

OFET: Organic Field-Effect Transistors

p6P: para-hexaphenylene

PMMA: Poly (methyl methacrylate)

SAM: Self-Assemble Monolayer

SDU: University of Southern Denmark

SEM: Scanning Electron Microscopy

SFIL: Step and Flash Imprint Lithography

SiO_2: Silicon Dioxide

TEM: Transmission Electron Microscopy

UV: Ultra-Violet

CHAPTER 1

INTRODUCTION

Our world is experiencing a technological revolution and we are becoming more and more dependent on technology. Technology could be defined as a way of using the knowledge about nature to develop techniques to control certain properties and thus create new ways for improving well-being. One of the technology branches is electronics, which had a huge impact in our lives in many different areas, as for example information, communication, health care, security, entertainment, etc.

Electronic devices developed with microfabrication silicon-based technology have been used in practically all products of the electronics industry. It is well-known that this is an extremely dynamic sector, which plays a very important role in the world's economy. One of the reasons for the microelectronics industry to have silicon as its main semiconductor material is that it presents a native oxide (SiO_2) which enables the formation of high quality semiconductor/insulator interfaces, which is fundamental for integrated circuits fabrication.

The advances within this area make technology more present in the people's lives, since the fabrication costs and energy usage are reduced at the same time the device performance is improved.

One type of devices that form part of our electronics technology consists of optoelectronic devices, including for example LEDs, lasers and photodetectors. Integration of optoelectronics functionality [1] with silicon-based technology is of high interest due to the advanced technologies available for silicon processing. However, they are often difficult to realize in silicon due to its indirect bandgap.

The combination of bottom-up and top-down technologies leads to a range of new device functionalities by integrating new materials into conventional silicon microsystem technology. For example, optoelectronic devices can be made possible by integration of nanowires made from inorganic semiconductors with direct bandgaps such as III-V or II-VI materials [2]. This has made possible both active [3-5] and passive [6] optoelectronics and photonic components. In addition, such nanostructures can function as advanced bio-sensors based on evanescent wave sensing due to their subwavelength cross-sectional dimensions [7] and for miniaturized, on-chip applications such as optical detection in lab-on-a-chip systems.

Much attention has being given to inorganic nanowires, both in terms of proof-of-principle optoelectronic devices like LEDs [8], lasers [4], and photodetectors [9] and also in terms of development of large-scale integration methods such as transfer printing [10] and in-situ growth [11]. The organic counterparts, however, have so far received less attention despite several unique advantages such as inherent tunability by the ability to tailor molecules for specific applications through synthetic chemistry [12-13], relatively low material cost, low temperature processing, and potentially high efficiency [14].

Typically, the integration of inorganic nanowires into silicon technology is done by first fabricating the nanowires on an appropriate growth substrate, followed by a transfer process to the silicon platform and additional processing to create the necessary interface [10, 15]. Although large-scale assembly has recently been demonstrated with such methodology [10], it is restricted to planar geometries and requires the use of special donor substrates. An alternative technique is in-situ growth, in which the nanowires are fabricated directly on the silicon substrate typically using catalyst nanoparticles to define nanowire diameter and position [16]. Despite problems regarding lattice mismatch and differences in crystal structure and thermal expansion coefficients, III-V nanowires can be grown epitaxially on silicon [17] enabling, for example, nanowire LEDs [18].

It has been shown that organic semiconductors can be formed into nanoscale, elongated, crystalline structures – 'nanofibers' – through bottom-up methods [19-20]. For example, *para*-hexaphenylene (p6P) molecules can self-assemble into lateral nanofiber structures by physical vapor deposition onto a heated mica substrate [19]. Such p6P nanofibers exhibit a range of functional properties such as emission of polarized, blue light through photoluminescence [21], waveguiding [22], and lasing [23], while electrical connection to the nanofibers [24] could enable OLED applications. In addition, by modifying the molecular building blocks, the nanofiber properties can be engineered for a particular application for example tuning of the emission spectrum [21] or color conversion through frequency doubling [25].

The standard substrate for the nanofiber growth is the mineral muscovite mica [19]. On this substrate, a dipole-induced interaction between the molecules and the substrate causes the nanofibers to grow along one of the high-symmetry directions of the mica surface, and the nanofibers are therefore straight and mutually parallel. However, as further processing of mica is not practical, the nanofibers need to be transferred to another platform for device applications, conceptually similar to the transfer strategy for the inorganic nanowires. However, large-scale device fabrication requires efficient placement and integration methods, which are up to now missing for organic nanofibers due to the soft and fragile nature of such van der Waals bonded molecular crystals [26]. In-situ growth would therefore constitute a highly interesting alternative. This requires that a suitable growth substrate is identified and a method for nanofiber growth control is developed. It has been shown that thin gold films constitute an alternative nanofiber growth platform, albeit without mutual alignment of the nanofibers [27]. If the substrate surface is structured on the micrometer scale, however, the nanofibers growth orientation will be affected by the microstructures [28]. The use of gold coated silicon platforms as the growth substrate is very beneficial, since the processing technology for silicon structuring is highly developed and advanced growth substrates can therefore be fabricated.

The objective of this Ph.D. project is to explore the possibility to control the length, orientation and position of p6P nanofibers grown on gold and to achieve directed in-situ growth of organic nanofibers into a device platform. A second objective is to achieve large scale fabrication of such devices by using nano-imprint lithography.

The description of the research background for nanofiber growth in different substrates is presented in the second chapter. Afterwards, the nanofiber growth controlled by nanostructures fabricated on the gold substrate will be explained (chapter 3), followed by a description of the devices feasibility on chapter 4 and finally, the implemented devices and results (chapter 5). The large-scale fabrication by nano-imprint lithography is discussed on chapter 6.

CHAPTER 2

BACKGROUND: NANOFIBER GROWTH

2.1 NANOFIBER GROWTH ON MICA

Para-hexaphenylene (p6P), $C_{36}H_{26}$, is a rod-like molecule consisting of six phenyl rings, as shown in Figure 1. It is a promising candidate for the electroactive layer in organic colored LED displays, due to its blue luminescence with high quantum yield [29]. The luminescence and the optical absorption of crystalline p6P are polarized along the long axis of the molecules. In the bulk form, the molecules are packed with the molecular axes parallel to each other [30]. Close packed faces are for example the $(1\underline{11})$, $(2\underline{11})$, $(30\underline{2})$ and (100) planes.

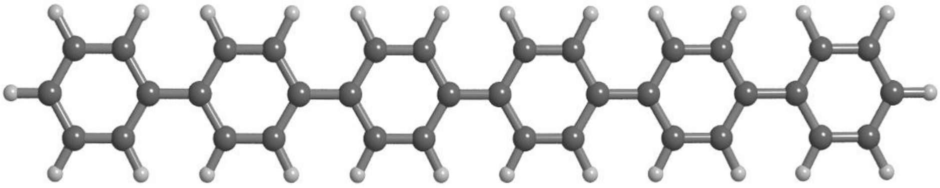

Figure 1: p6P molecule structure

These molecules can be evaporated in ultra-high vacuum by molecular beam Knudsen sources. By depositing p6P on different substrates, the molecules can be either lying or standing upright on the substrate surface, and can form either continuous films or needle-like p6P aggregates, depending of the substrate chemical and physical properties. Thin films of p6P were initially deposited on GaAs, glass, indium thin oxide (ITO) or KCl [31-33]. By depositing p6P on GaAs (001)-2x4, needle-like islands were formed [34-35]. Later experiments have shown that large scale, mutually parallel p6P needle-like structures could be grown by hot-wall epitaxy on fleshly cleaved muscovite mica [36]. Muscovite mica was chosen in the first place as substrate material since the extremely small surface roughness of the substrate does not mask the intrinsic features of the deposited film. The resulting needles are crystalline [37], and interesting for their waveguide character [22] and for their potential as connectors in optoelectronic devices.

Muscovite mica is a sheet silicate consisting of consecutive layers of K, Al, SiO_4 and OH [38]. The potassium ions have weak bounds to the sheet plane, and therefore, muscovite mica is cleavable at the potassium planes (see Figure 2).

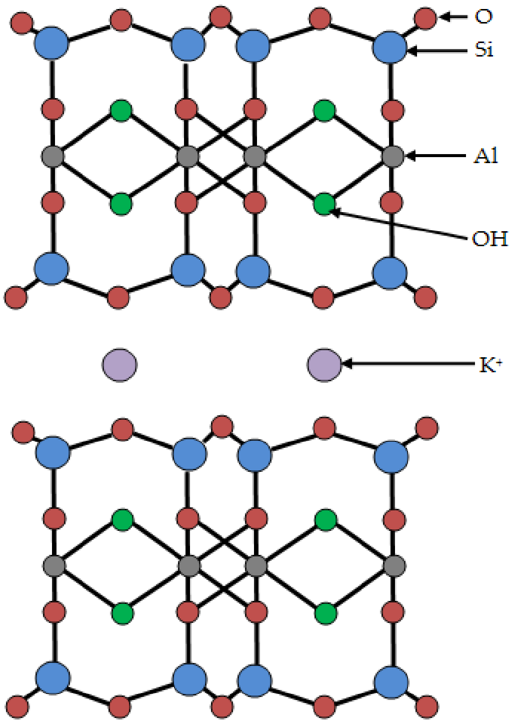

Figure 2: Crystalline structure of muscovite mica (adapted from [38])

During cleavage, half of the potassium ions are removed from the surface [19]. The remaining half-monolayer potassium ions plus the equal number of substutional aluminum ions form surface dipoles in freshly cleaved mica. The axes of these dipoles are rotated by about 15^0 with respect to the surface unit vectors. The driving forces for the oriented growth of nanofibers is a combination of the interaction of the p6P molecules to these dipole fields created on the mica surface and to the grooves on the dioctahedral [39] muscovite mice surface. Upon p6P deposition on the mica substrate, the p6P molecules first form a wetting layer of lying molecules, growing with their close packed $(1\underline{11})$ and $(2\underline{11})$ faces parallel to the substrate, self-assembling and forming the nanofibers. The bonding strength between the p6P molecules is higher in the long nanofiber axis and weaker in the long axis of the individual p6P molecules, which causes the organic nanostructures to have the needle shape. The orientation angle of the molecules axes is very close to the orientation angle of the surface dipoles.

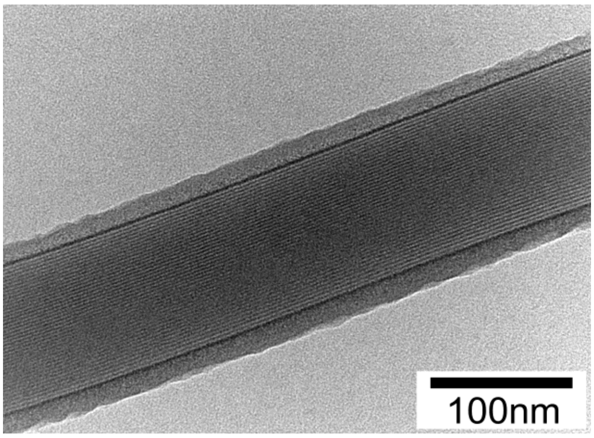

Figure 3: TEM image of a single nanofiber, showing the well-oriented molecular planes [courtesy Annette Thierry NRS-2004].

The resulting individual fibers are crystalline, as shown on Figure 3, which is a Transmission Electron Microscopy (TEM) image of an individual nanofiber, showing the well-alligned molecular planes. The typical dimensions for the nanofibers are illustrated in Figure 4, which is an Atomic Force Microscopy (AFM) image of a nanofiber. The deposited p6P thickness is also an important parameter to the nanofibers morphology. For the nominal thickness of 4 nm, the typical dimensions are a height of about 80 nm and a width of 150 nm. Adittionally, the nanofiber length is strongly dependent of the substrate temperature, as will be discussed later.

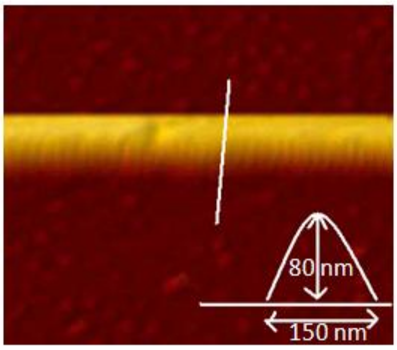

Figure 4: AFM image (1μm x1 μm) of a nanofiber grown on mica, showing the typical dimensions [adapted from 40].

The resulting nanofibers emmit polarized blue light when excited with UV-light (Figure 5), with the polarization vector parallel to the long molecular axis and thus almos perpendicular to the long needle axis.

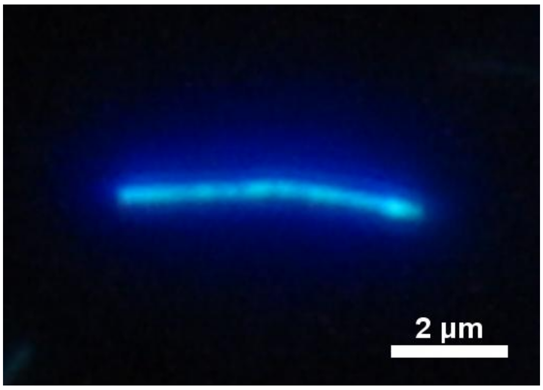

Figure 5: Fluorescence microscopy image of a nanofiber excited with UV light.

For nanofiber growth with the substrate temperature set to room temperature, the resulting fibers are only a few ten nanometers long. However, the nanofiber length depends very much on the muscovite mica surface temperature during p6P deposition. For a certain p6P thickness, the length of the nanofibers increases with increasing surface temperature. Figure 6 shows fluorescence microscopy images of p6P nanofibers grown on mica at three different temperatures. One can observe that the nanofibers are shorter and more dense for lower temperatures, and grow longer when the temperature is increased, until a critical temperature is reached. This is due to the diffusion coefficient for the molecules, which increases when the surface temperature is increased, causing the molecules to diffuse over a longer path and form longer fibers. For higher temperatures than the critical temperature, the p6P molecules do not stick to the surface any longer, and there is not nanofiber formation.

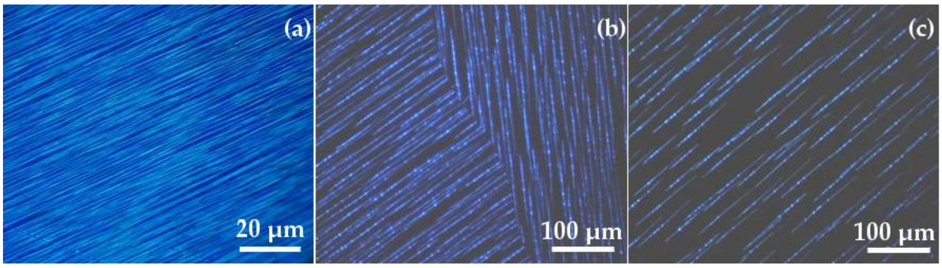

Figure 6: Fluorescence image of nanofibers grown on mica at substrate temperatures of (a) 440 K (b) 450 K and (c) 455 K [41]

2.2 NANOFIBER GROWTH ON PLANAR GOLD

Under the optimum conditions, p6P deposition on mica generates nanofibers, and the resulting fibers are long, straight and mutually parallel. However, muscovite mica is fragile and not further processable. For the use of fibers in optoelectronic devices, electrical contacts to the fibers are essential. One possible approach is to grow the fibers directly on electrodes made of for example a thin Au layer.

The first experiments were made by depositing a thin gold film on mica before p6P deposition, in order to determine its influence on the nanofiber growth [27]. Initially, 3 nm of p6P were deposited on plane muscovite mica and on mica covered with 2 and 5 nm Au. Mutually parallel fibers were observed, but the average nanofiber length and the degree to which the fibers are mutually parallel decreases with increasing the gold thickness. Besides the length, the heights and widths are also affected by the gold layers because there is a change on the interface energies (Figure 7).

The trend was also reproduced for thicker p6P nominal thicknesses. Small p6P clusters were also observed along with the nanofibers on these samples. The clusters are believed to form the fibers by agglomeration. Even for 5 nm Au, the fibers still follow a preferred orientation, which shows that it is a long range interaction which determines the alignment (electrical fields on the surface).

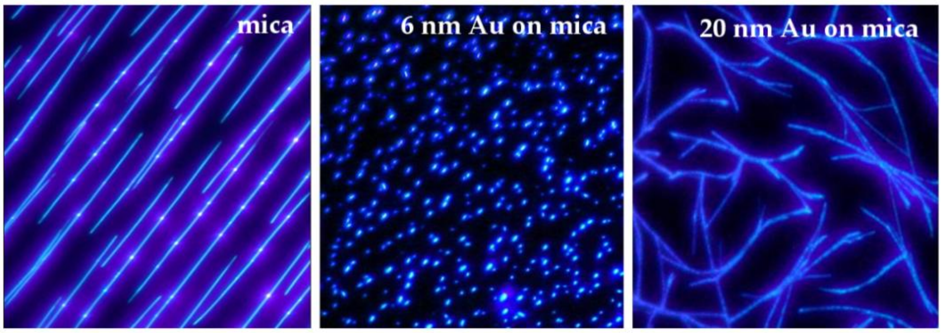

Figure 7: Fluorescence microscopy image of nanofibers grown on different substrates (100 μm x 100 μm) [27].

Increasing the gold thickness to 8 and 17 nm, the nanofibers morphology becomes more influenced by the gold film and its (111) orientation than by the underlaying muscovite mica. When the gold thickness is around 8 nm, the nanofibers reach their minimum length, and for thicker gold layers, the length starts to increase again. However, the fibers are no longer aligned and parallel, since the dipole field from the underlaying mica does not affect the p6P molecules anymore and the epitaxial relationship between muscovite mica and p6P crystals gets lost. The difference in morphology for fibers grown on a very thin gold film and on a thicker gold film is due to the gold film homogeneity, which is better in the thicker film. This determines the mobility of the p6P molecules on the surface, which can diffuse longer on a more homogeneous film.

The surface energy is very important for the resulting nanofibers morphology, since it influences the molecular arrangement in the nanofibers. The surface energy of freshly cleaved mica in vacuum is around 5000 mJ m^{-2} [42], while it is around 1400 mJ m^{-2} for gold [43]. Therefore, the aggregates height first increases when the Au thickness is increased, until the thickness of 8 nm Au is reached (when the surface energy of the mica can still be felt) and remains constant for thicker films, since the surface energy remains constant to the values for gold. However, when the gold thickness is more than 8 nm, facets along the long needle axis show up.

Assuming that for thicker gold films the dipole fields for the underlaying mica are not influencing anymore, one could assume that the gold film could be deposited on any kind of substrate, including silicon, which is the standard substrate in microelectronics, and therefore, is a promising substrate for nanofiber device implementation. Experiments were made by depositing a 20 nm gold film on silicon, followed by p6P deposition. Figure 8 are fluorescence microscopy images of the resulting fibers. One can observe that their morphology is very similar to the fibers grown on the gold film on mica.

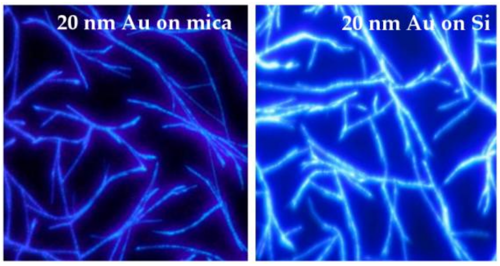

Figure 8: Fluorescence microscopy images for nanofiber growth on gold film on mica and silicon (100 μm x 100 μm) [27].

2.3 NANOFIBER GROWTH ON STRUCTURED GOLD

In the last section, the nanofiber growth on gold films was discussed. The fibers are long, but do not present the same alignment observed for the fibers grown on plane mica. The nanofiber growth on artificially made templates on gold surfaces is an option for controlling the nanofiber growth direction.

A first attempt was made by growing nanofibers on Au-coated porous alumina templates [44]. Nanofiber growth was observed and the nanofibers possessed heights and widths of one hundred and a few hundred nanometers, respectively, and lengths from a few to a few tens micrometers. In addition, the nanofibers present the same faceted morphology as observed for the nanofibers grown on plane gold surfaces. Figure 9 is a Scanning Electron Microscopy (SEM) image of p6P nanofibers grown on a gold coated alumina template. The pore size and order apparently have an ordering effect on the growth process. Based on this, new approaches for substrate templates were made.

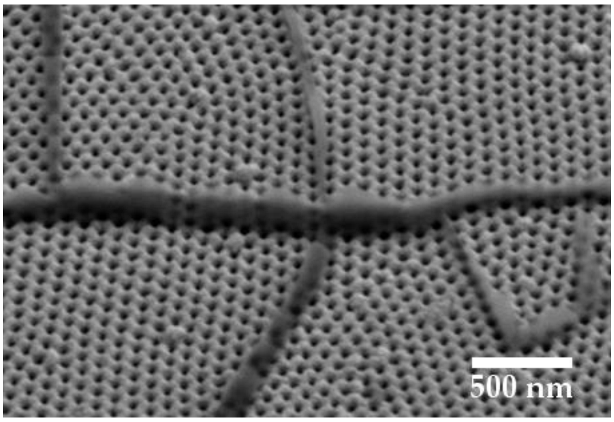

Figure 9: SEM image of p6P nanofibers grown on gold coated alumina templates [40]

The second approach consisted of micro-structured silicon substrates coated with a thin gold film to enable molecular diffusion, which is hindered on Si [45-46]. Silicon was chosen since well-established techniques exist for silicon processing. Periodic micro-ridges were fabricated in silicon by standard optical lithography and reactive ion etching. The substrate was then covered by a 55 nm gold film.

Upon deposition of p6P molecules on the micro-structured gold substrates, nanofibers are formed all over the gold, and also on the micro-ridges. Different substrate temperatures during p6P deposition lead to differences on the nanofibers density, length and orientation. Figure 10 shows SEM images of 5 nm p6P deposited on 2.5 μm wide ridges at 388 K (a) and 435 K (b), respectively. Upon landing on the substrate, the molecules undergo diffusional motion, cluster together, and grow into the nanofiber structures.

Since the molecular diffusion is temperature dependent, the results from the experiments performed at different temperatures are distinctly different (Figure 10 a and b). Clearly, the nanofiber density is higher and the fibers are shorter at low substrate temperatures where the diffusional range is relatively short, as it is the case for nanofibers grown on mica [47]. When depositing molecules on a structured substrate, the ridge edge causes the nanofiber nucleation to start from there. At low temperature (Figure 10a), the nanofibers on the ridges seem to have a preferred orientation perpendicular to the long ridge axis. At higher temperatures, this effect is more pronounced and the nanofibers tend to grow perpendicular to the long ridge axes, and the length is determined by the ridge width (Figure 10b), since the diffusional motion is increased.

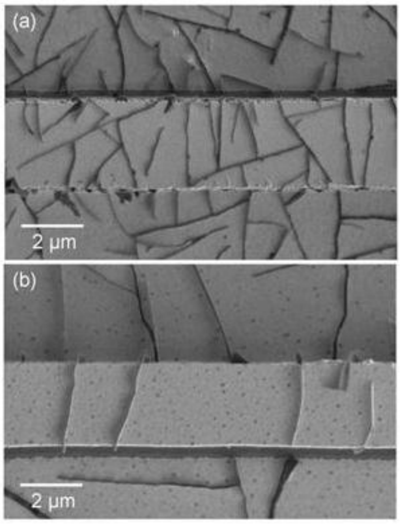

Figure 10: SEM images of p6P nanofibers grown on gold coated micro-scaled ridges at 388 K (a) and 435 K (b) [46].

This method can control the length and orientation of in-situ grown nanofibers on gold surfaces. In this project, the nanofiber length and orientation is controlled by nanostructures fabricated on gold surfaces.

2.4 CHAPTER SUMMARY

This chapter gives an overview on the previous work to the approaches presented in this thesis. From the first observation of p6P nanofibers self-assembled by p6P deposition on different substrates, muscovite mica has shown to be the substrate for nanofiber growth which results in well-aligned, mutually parallel and long nanofibers. However, further processing of mica is impractical, which leads to the necessity of investigation of alternative substrates. One of these consists of a gold film, deposited on any substrate, which has advantages on the technological point of view, where the fibers could grow directly on the device platform.

However, the resulting fibers are no longer aligned and parallel when deposited on gold. Further investigations have shown that it is possible to control the nanofiber lengths and directions by including gold coated micro-ridges on the gold surface.

CHAPTER 3

NANOFIBER GROWTH ON NANO-STRUCTURED GOLD

In a further development for the method of growing nanofibers on micro-structured gold, the investigation of nanofiber growth on gold surfaces containing nanoscaled structures was performed. One of the advantages of using nano-structures instead of micro-structures is that more design variations are possible. Since the maximum nanofiber length is of the order of 400 μm, this value should be considered as the maximum diffusion length for the p6P molecules. The diffusion length is an important parameter to be considered when we design the growth substrates.

In this chapter, a method for controlling orientation, length and position of the in-situ grown nanofibers is presented.

3.1 ORIENTATION AND LENGTH CONTROL

In this section the nanofiber orientation and length control by using pinning lines is presented. These lines consist of ultrathin, nanoscale titanium lines on a gold coated silicon substrate (with different pitch distances) [48], thus avoiding the necessity to fabricate grooves into the substrates.

3.1.1 EXPERIMENTAL

The nanofiber growth platform consists of Silicon (100) substrates, which initially were coated with a 5 nm Ti adhesion layer deposited by electron-beam deposition and a 60 nm thick Au film deposited by electron-beam deposition (rate: 2 Å/s, background pressure in the 10^{-6} mbar range) or by DC sputtering (rate: 5 Å/s, pressure in the 10^{-3} mbar range). Nanoscale titanium lines were fabricated by electron beam lithography, titanium deposition, and lift-off: 150 nm PMMA was applied by spin coating, and the electron beam lithography was performed at 30 keV in a Hitachi S-4800 SEM with a Raith ELPHY Quantum module. After exposure, the pattern was developed by immersion in a 3:1 IPA:MIBK solution, rinsed, and dried, followed by Ti deposition (rate 1 Å/s, background pressure in the 10^{-6} mbar range). Different thicknesses of Ti were used in order to study the Ti height influence. The resist was lifted off by immersing the samples in a Remover PG solution and applying ultrasonic agitation. Before deposition of p6P molecules, the samples were cleaned with a mild oxygen plasma to remove any organic residues.

Organic nanofibers were grown on the nano-structured substrates by physical vapor deposition of p6P molecules at a rate of 0.1 Å/s. During deposition, the substrate was heated to temperatures in the range 418 – 448 K and the deposition was performed under high vacuum conditions (10^{-8} mbar). The organic material is deposited from a Knudsen cell, and the p6P thickness was changed from sample to sample to study its influence on growth control.

3.1.2 RESULTS AND DISCUSSION

Results are presented from a systematic investigation of the influence of various processing parameters such as pinning line dimensions, pitch distance, substrate temperature and p6P thickness on the nanofibers alignment, length and position control. From this study we determine optimum parameters for pinning of the growth.

Upon deposition of p6P molecules on the nanostructured substrates, the nanofibers are investigated with scanning electron microscopy (SEM). Figure 11 a and b show SEM images of nanofibers grown on a gold film by deposition of 4 nm p6P at substrate temperatures of 418 K (Figure 11a) and 448 K (Figure 11b), respectively. The pinning lines have a width of 250 nm and a height of 25 nm. The pitch distance varies between 2.5 μm (label '1' in figure 14a) and 17.5 μm (label '7').

The deposited p6P molecules undergo diffusional motion on the heated gold surface until they reach a pinning line, causing the nanofibers to grow from the line. Different deposition conditions such as different substrate temperatures lead to distinct differences in the orientation and morphology of the resulting nanofibers. As observed from the SEM images, the fibers grow longer if the deposition is performed at a higher substrate temperature since the diffusional range is increased. The nanofibers length is also influenced by the pinning lines pitch distance. Under appropriate conditions, the nanofibers bridge between two lines and length control can thereby be achieved as shown in Figure 12.

The fiber orientation is another characteristic property affected by the growth conditions. The fibers grown on a high temperature substrate exhibit a better alignment, i.e. they grow more perpendicular to the pinning lines. This effect has been observed also for nanofibers growing on or between micro-structures. At high temperatures, most fibers grow from the pinning lines even for long pitch distances. At lower temperatures and long pitch distances, some fibers nucleate in between and are thereby disconnected from the lines, which results in a decrease of the alignment factor.

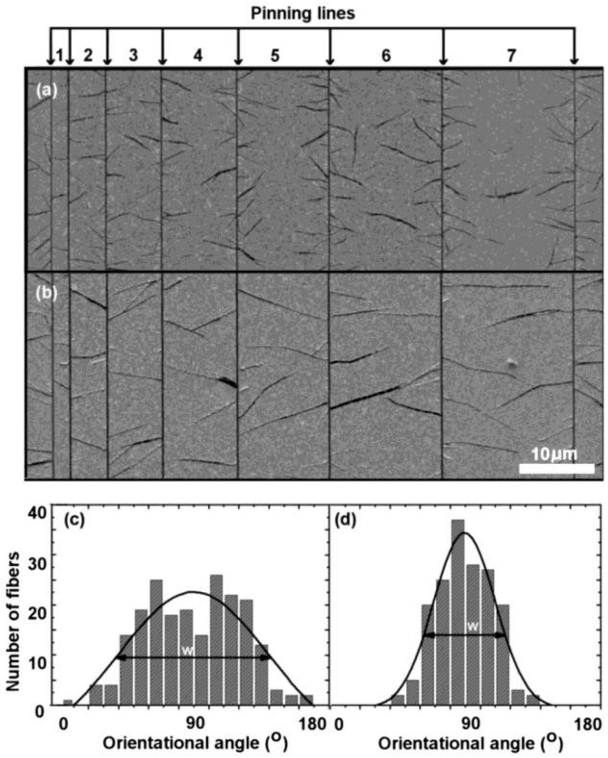

Figure 11: (a and b) SEM images of p6P nanofibers grown on sputtered gold with titanium pinning lines (width of 250 nm and height of 25 nm) at substrate temperatures of 418 K (a) and 448 K (b), respectively. The distances between the lines are 2.5 µm (1), 5 µm (2) … 17.5 µm (7); (c and d) orientational distributions for the fibers growing between lines at a pitch distance of 10 µm (4) for substrate temperatures of 418 K (c) and 448 K (d), respectively. Here, 90 degrees refers to the long fiber axes being perpendicular to the pinning lines.

Systematic analyses with the objective of obtaining quantitative data for the fiber’s alignment were made by measuring their angle with respect to the pinning line direction. 90˚ refers to fibers oriented perpendicularly to the pinning lines. The orientational distributions corresponding to the fibers grown at a pitch distance of 10 µm (label ‘4’ in Figure 11a) at 418 K and at 448 K are plotted in Figure 11c and d, respectively. As seen, the width of the distribution is narrower for fibers grown at a high temperature as compared to those grown at a low temperature.

Another factor affecting the nanofiber growth is the quality of the gold, which is influenced by the deposition method. Figure 13a and b show SEM images of nanofibers grown from titanium pinning lines on a gold film that had been deposited by DC sputtering and electron beam evaporation, respectively, while Figure 13c shows a SEM image of nanofibers grown on a sputter deposited gold film without pinning lines (4 nm p6P deposition, substrate temperature of 418 K). The pinning line dimensions are the same as in Figure 11.

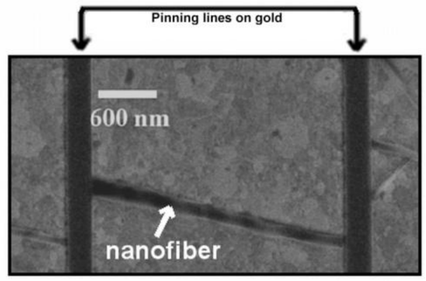

Figure 12: SEM image of a nanofiber bridge between two pinning lines (width of 250 nm and height of 50 nm) at a pitch distance of 2.5 μm. The substrate temperature during deposition of 4 nm p6P was 433 K.

The nanofiber lengths for the fibers grown between the 2.5 μm pitch distance lines for the samples presented in Figure 13a and b are plotted in the histograms in Figure 13d and e, respectively, while the length distribution on the unstructured film is shown in Figure 13f. The distributions illustrate that the pinning lines are indeed limiting the nanofiber lengths on both types of gold film, but the effect is more pronounced on the gold film that was deposited by sputtering. A better alignment to the pinning lines is observed on the sputter deposited film, while on the film deposited by evaporation, more fibers are not perpendicular to the pinning lines, making it possible to grow longer. Figure 14 shows 3D AFM images of 60 nm of Au deposited on Si by evaporation (Figure 14b) and by sputtering (Figure 14a). An analysis of the surface roughness shows that the evaporated gold film has a 20% larger surface roughness than the sputtered film. We propose that this is affecting the diffusional motion of the molecules and that it could cause the observed difference. However, we do not attribute the difference on surface roughness only to the deposition method, but also to the deposition system condition. In further experiments (next chapters), the gold films deposited by e-beam evaporation presented similar quality to the films deposited by sputtering, since changes on the e-beam evaporation system were made to improve the deposition quality.

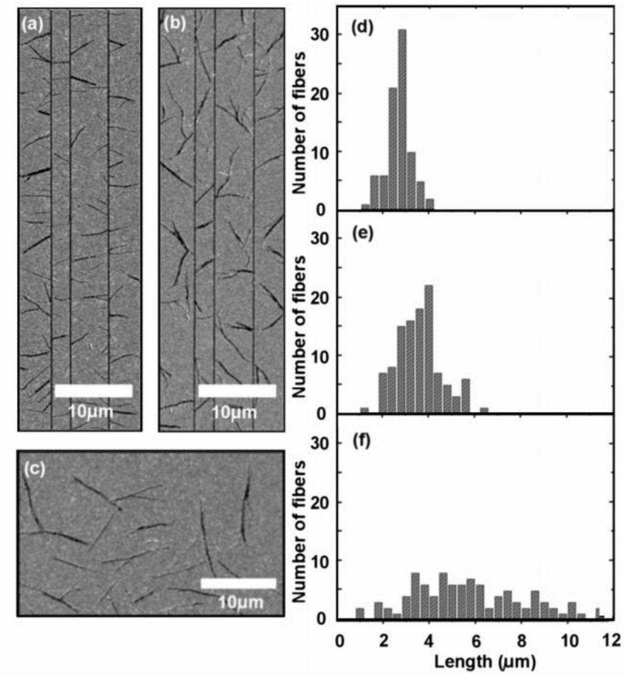

Figure 13: (a and b) SEM image of p6P nanofibers grown on a sputtered (a) and e-beam evaporated (b) gold film with titanium pinning lines (width 250nm and height 50 nm), respectively, at a substrate temperature of 418 K; (c) SEM image of p6P nanofibers grown on a sputtered gold film without pinning lines at a substrate temperature of 418 K; (d-f) length distribution for the fibers grown between pinning lines (separation 2.5 µm) on the samples shown in (a and b) and for the substrate shown in (c), respectively.

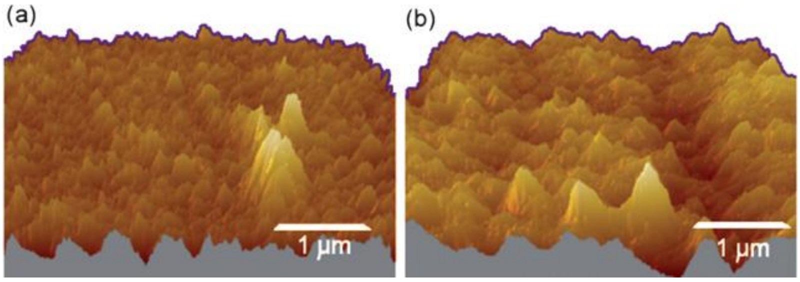

Figure 14: AFM image of a gold film deposited by sputtering (a) and e-beam evaporation (b). The maximum z-range is 3.8 nm.

The ability of the pinning lines to control the nanofiber length is also demonstrated in Figure 13. In order to compare to nanofibers grown on an unstructured gold film, Figure 13c displays such nanofibers grown under the same conditions as the fibers in Figure 13a. The length distribution for these fibers is very wide (Figure 13f), since this is a statistical process without any limiting factors and there is therefore no length control. The improvement of length control can be seen comparing Figure 13d and f, where the length distribution is significantly narrower for the former case.

The morphology of the nanofibers has been investigated by atomic force microscopy (AFM). Figure 15 show a 3-D AFM image of a single p6P nanofiber grown between two nano-scale titanium lines with a pitch distance of 2.5 μm.

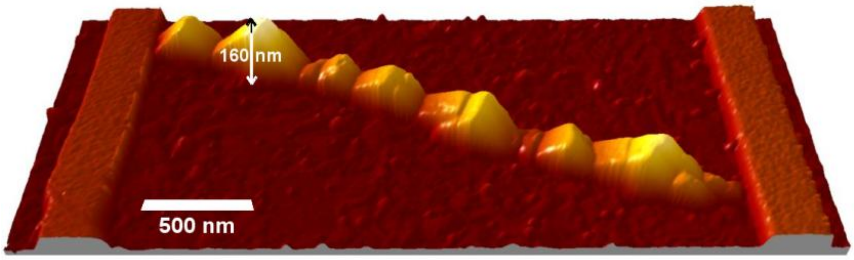

Figure 15: AFM image of a single nanofiber grown between two pinning lines, separated by a distance of 2.5 μm. The nanofiber is grown at a substrate temperature of 433 K.

The nanofiber is grown at a substrate temperature of 433 K. The nanofiber show a faceted morphology, which is normally seen for nanofibers grown on gold. The maximum height of the nanofiber is around 160 nm, whereas its width is around 200 nm. These dimensions are similar to those previously reported for nanofibers grown on planar gold surfaces and gold-coated micro-scale ridges under similar conditions. The length of the nanofiber grown between the titanium lines is limited by the distance between the lines, and is around 2.8 μm, since it is not grown completely perpendicular to the lines in this case. Furthermore, clusters from which the nanofibers are assembled are probably seen around the nanofibers. Note that although the nanofibers are much higher than the titanium lines, the nanofibers do not grow across them, because p6P diffusion is hindered.

Figure 16 and Figure 17 shows how the various processing parameters affect the nanofibers. In the first row, the average lengths for the fibers are shown with the different processing parameters varied on the different columns. The fibers orientation as a function of the parameters is plotted in the second row. Here, it is plotted as 100 divided by the standard deviation of the orientational distribution. In this way, the fibers orientation factor is increasing when the alignment is improved. The characteristic shown in the last row is the pinning factor (position control), which is defined as:

$$PC = Nc/(Nnc + Nc),$$

with Nc being the number of nanofibers connected to a pinning line and Nnc being the number of fibers not connected.

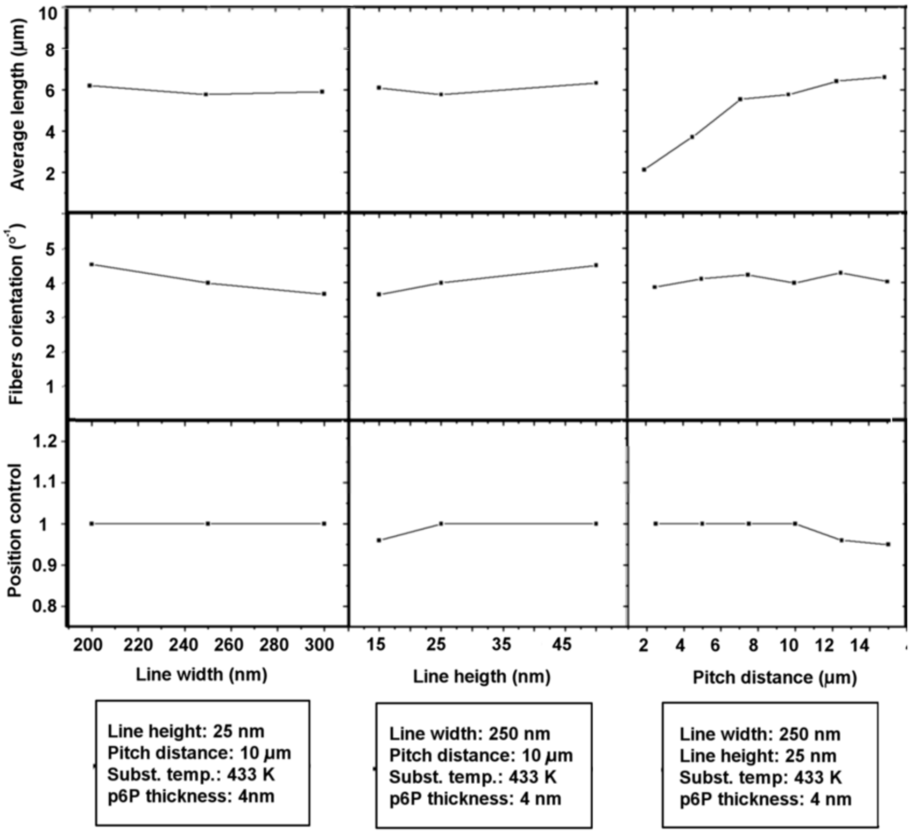

Figure 16: Nanofiber average length, orientation, and position control as a function of substrate parameters.

Each column shows the results of one of the processing parameters being varied, while all the other parameters are fixed to the mean values. The plot shows data obtained from the samples with the gold film deposited by sputtering. Similar trends are observed for the e-beam evaporated gold, but the sputtered samples display better results in terms of alignment, and position and length control.

As observed from the first column, the line width does not have a significant influence on most of the parameters, except for a slightly decreasing fiber orientation for increasing line width. The opposite trend is observed for increasing line height (second column), in which case the fibers exhibit a better orientation. This indicates that the optimum conditions are lines with a large aspect ratio. The pitch distance factor is crucial for the nanofiber length as well for the position control, since for large areas in between pinning lines, some of the molecules do not have sufficient thermal energy to diffuse to the lines, and fibers are grown disconnected from the lines. The effect of the pitch distance is to determine the average length of the nanofibers, since the fibers lengths are limited by the available space in between two pinning lines. If the pitch distance is small enough, length control can be achieved.

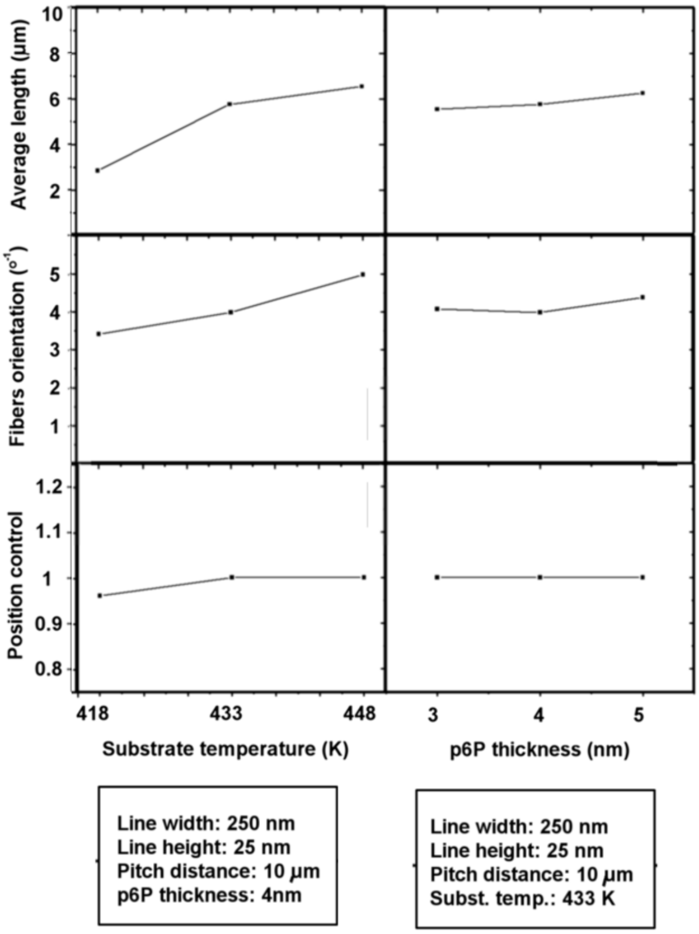

Figure 17: Nanofiber average length, orientation, and position control as a function of growth parameters.

The substrate temperature is an essential parameter since it influences length, alignment and position control, while the p6P thickness does not have a significant influence. It has been shown that there is a maximum substrate temperature for nanofiber growth, which is around 450K. At the highest temperature used here (448 K), the standard deviation of the orientational distribution is 19°. This could be compared to nanofibers grown on mica, in which the epitaxial relation with the substrate causes a mutual alignment of the nanofibers with a standard deviation of the angular distribution of just 1.2°. However, as previously noted, any processing on mica is practically impossible rendering the silicon-based platform the preferred choice for in-situ growth experiments despite the inferior nanofiber alignment properties. In addition, the use of pinning lines also enables length control on the silicon-based platform, which is not possible on plain mica, where the length distribution function is similar to that on plain Au.

The p6P molecules emit blue light upon UV excitation with the emitted photons polarized along the long molecular axes. In the nanofiber crystal structure, the molecules are mutually parallel and aligned almost perpendicular to the long nanofiber axis. The photoluminescence output from the nanofibers is therefore also polarized approximately perpendicular to the long nanofiber axis.

Figure 18 illustrates how this property causes the emitted light from the aligned nanofibers to be polarized. The nanofibers are grown on an array of pinning lines with a pitch distance of 2.5 μm, as illustrated in Figure 18a. The pinning lines are vertical with a width of 250 nm while their heights are 25 nm. The deposition of 4 nm p6P was performed at a substrate temperature of 433 K, forming nanofibers perpendicular to the lines, as shown in Figure 18b. Figure 18c and d show epifluorescence microscopy images of nanofibers illuminated with unpolarized light and imaged through a polarizer. In Figure 18c, the polarizer direction is horizontal while in Figure 18d the direction is vertical. When the polarizer is rotated for observation of light polarized approximately parallel to the long nanofiber axes, only minor light emission is observed, however, rotating the polarizer by 90° causes a significant increase in the observed light intensity. This indicates that the light-emitting molecules are oriented all perpendicular to the long nanofiber axes and thus parallel to the pinning lines. The pinning lines allow one thus to fabricate areas with well defined polarization on samples that otherwise emit unpolarized light.

The same effects observed for the fibers grown on the micro-structures shown on chapter 2, were observed for the fibers grown on a gold film with nano-scale pinning lines, fabricated with a separation distance of 2.5 μm to allow for direct comparison with the ridges. As the nanofibers do not grow on the titanium lines, the fibers are formed in the space between the lines, and, under the right conditions, bridge and connect the lines.

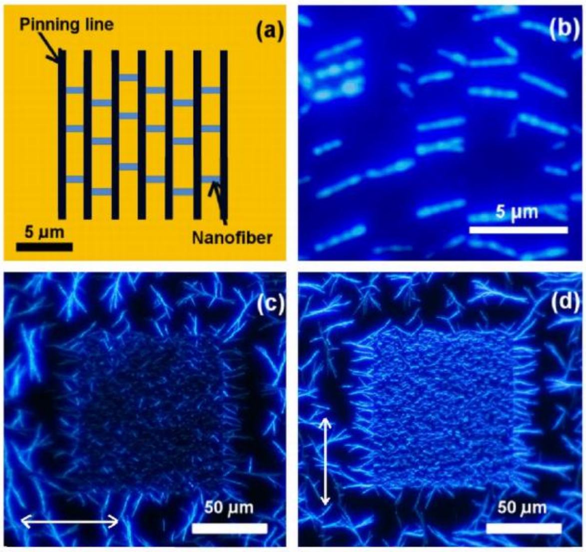

Figure 18: (a) Outline of sample geometry: parallel pinning lines (width of 250nm and height of 25nm) with a pitch distance of 2.5 µm; (b) fluorescence microscopy images of p6P nanofibers grown at substrate temperature of 433 K; (c and d) The nanofibers are illuminated with unpolarized light and imaged trough a polarizer. The polarizer direction is parallel (c) and perpendicular (d) to the long lines axis as indicated by the arrows.

Figure 19a shows the orientational distributions for fibers grown on ridges and in between pinning lines at substrate temperatures of 435 K and 433 K, respectively. The difference in the temperature for the two samples is within the uncertainty of the measurements, and is therefore assumed to be negligible. The distributions are very similar, which clearly demonstrates that the control of the nanofiber orientational distribution can also be obtained through the use of nano-scale pinning lines. The standard deviation for the orientational distribution is 24.1 degrees for the nano-scale pinning lines and 25.6 degrees for the micron-size ridges. Similar to the micron-size ridges, the pinning lines also influence the nanofiber length as shown in Figure 19b.

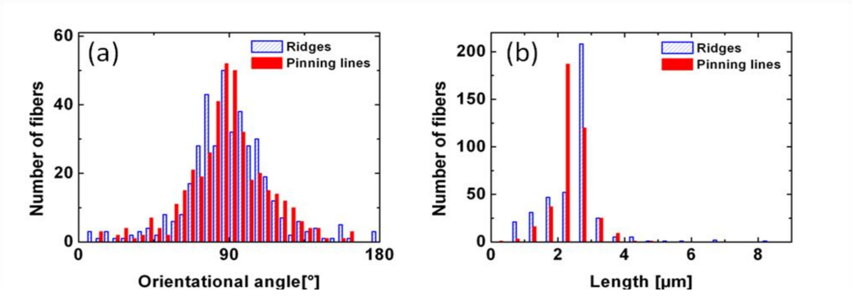

Figure 19: Comparison between (a) orientational and (b) length distributions of nanofibers grown on 2.5 µm wide ridges and nano-scale pinning lines (with 2.5 µm separation distance), respectively [46].

3.2 DESIGN VARIATIONS

In the previous section, the nanofiber length and orientation growth by taking use of titanium pinning lines fabricated on gold was demonstrated. In order to control the position of in-situ grown nanofibers, further development of the pinning lines design was performed, by introducing nano-scale nucleation points in the line edge [49], as shown in Figure 20a. Another developed design modification was the one consisting of titanium gratings on gold, where the ratio between the line width and line gap is 1:1 (Figure 20b).

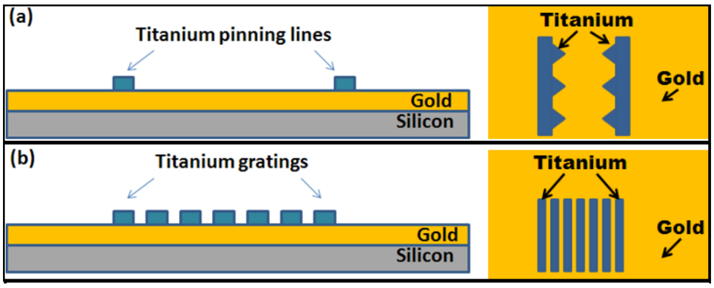

Figure 20: Cross-sectional view (left side) and top view (right side) of the different design modifications for the pinning lines (not to scale): (a) Design 1: titanium pinning lines containing nucleation structures on gold. (b) Design 2: titanium gratings on gold.

3.2.1 POSITION CONTROL

Only length and orientation of the nanofibers are controlled by using the pinning lines presented on the previous section. In order to try to achieve position control, small nucleation structures on the titanium line were added to the pinning line design. The molecules are then expected to be pinned to these nucleation structures to cause the nanofiber growth to start from there, since the nucleation structures are reducing the degree of freedom of the landing molecules and therefore hindering the diffusional motion.

3.2.1.1 EXPERIMENTAL

The substrates were prepared by initially coating a silicon substrate with gold (60 nm) by sputtering. Afterwards, electron beam lithography, using a Vistec VB6 UHR EWF system, was used to define the pinning lines or grating pattern, followed by titanium deposition and lift-off. The nanofiber growth was performed by vapor deposition of p6P molecules (thickness of 5 nm) onto heated substrates (175°C) under high vacuum conditions (~ 10^{-8} mbar). The nominal thickness and deposition rate (~ 0.1 Å/s) was monitored by a water-cooled quartz microbalance. The images of the as-grown nanofibers were obtained by SEM.

3.2.1.2 RESULTS AND DISCUSSION

Different configurations were made, containing various shapes of the nucleation structures (squares, triangles and circles) in order to investigate the influence of the nucleation structure morphology. Figure 21b and c are SEM images of pinning lines containing nucleation structures after p6P deposition. As can be seen from the images, in both cases the resulting nanofibers start to grow from the pinning lines, and additionally they grow from the nucleation structures on the outward pointing convex structures. The inward pointing concave structures do not seem to have a big influence on the nanofiber position.

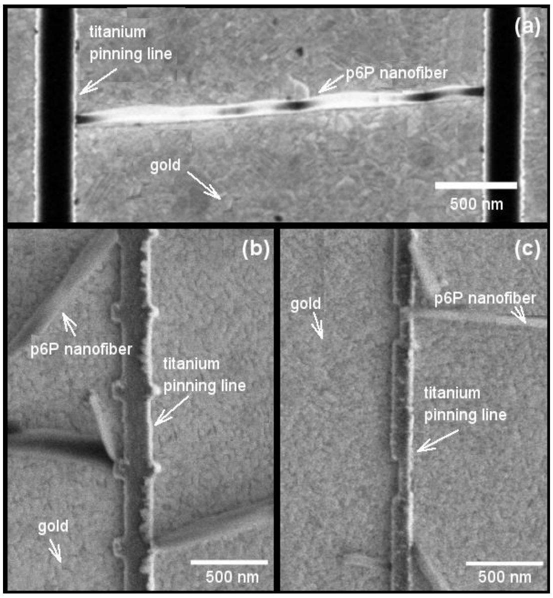

Figure 21: (a) p6P nanofiber grown directly on the substrate containing titanium pinning lines without nucleation structures. (b-c) More advanced pinning lines with nucleation structures pointing out from (b) or in to (c) the pinning line.

In order to quantify the influence of the nucleation structures on the nanofiber position, the number of fibers connected to the different types of nucleation structures was determined from SEM images. The statistics were made by taking into account about 350 fibers. The nucleation structures occupy

20 % of the total pinning line length, so it is expected that if the nucleation structures have no influence, statistically 20 % of the fibers should be connected to these structures. Figure 22 shows that for convex structures about 60 % of the fibers are connected to the points, demonstrating that position control can to some degree be achieved by introducing these structures. The concave seem to have no influence on the growth position, but the mechanisms leading to this behavior are here not fully understood.

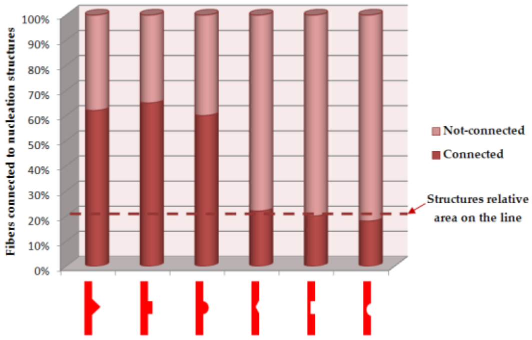

Figure 22: Diagram showing the percentage of nanofibers on a pinning line which are connected to a nucleation structure for different configurations. The nucleation structures occupy 20% of the total line length as indicated by a dashed line.

To obtain such position control opens the possibility to fabricate devices where the in-situ grown fibers occupy specific positions on the device. More about devices feasibility will be discussed on the next chapter.

3.2.2 NANOFIBER GROWTH ON METAL LINES

On the first design modification, the nanofibers have been formed from clusters that diffuse on the gold surface between the titanium lines. In order to investigate how the available gold surface area affects the nanofiber formation, we fabricated a growth substrate with similarly sized titanium lines but with a much smaller pitch distance (basically a grating), i.e. the gold surface area and the titanium surface area were approximately equal as shown previously on Figure 20b.

3.2.2.1 EXPERIMENTAL

The substrates fabrication process, nanofiber growth and characterization are the same presented on section 3.2.1.1.

3.2.2.2 RESULTS AND DISCUSSION

Figure 23 is a SEM image showing one of these gratings after deposition of p6P molecules.

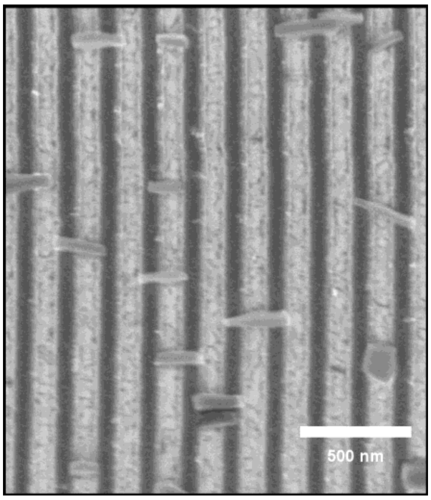

Figure 23: SEM image of p6P nanofibers grown on a titanium grating on gold with a pitch distance of 200 nm.

The difference of this structure to the grating structure shown in Figure 18 is the pitch distance, which is much smaller in the grating presented in this section (about 200 nm). Therefore, the organic nanostructures are formed also on the titanium lines and across them, which is very interesting, since there is not nanofiber formation on plane titanium films. In addition, the nanostructures are well aligned, perpendicular to the grating lines, and they present a different morphology than the nanofibers growing on gold surfaces with larger area for the molecules diffusion.

To grow the fibers on metal lines opens a lot of possibilities. It could be eventually grown on metal lines which are electrically isolated from the bulk substrate. Devices feasibility will be discussed in the next chapter.

3.3 CHAPTER SUMMARY

In this chapter, a method for controlling the orientation, length and position of in-situ grown nanofibers is presented. Nano-scale titanium lines are fabricated by e-beam lithography, metal deposition and lift-off on a gold-coated silicon substrate. Upon p6P deposition, nanofibers are formed on the gold surfaces, perpendicular to the titanium lines. The nanofiber length is determined by the pinning lines pitch distance, and the nanofibers position is controlled by nano-scale pinning structures fabricated on the pinning lines edges.

In addition, it is demonstrated that the nanofibers can be grown **on** the titanium lines, if the pitch distance is reduced to few hundred nanometers. The morphology of the resulting nanofibers is different than the one observed for the nanofibers grown on gratings with larger pitch distance, where the nanofibers are formed on the gold surfaces, and not on the titanium lines.

CHAPTER 4

IN-SITU GROWTH FOR ELECTRICAL CONNECTION

In order to perform electrical characterization on the grown nanofibers and to fabricate device platforms for nanofiber growth, it is necessary that both the device electrodes and the grown nanofibers are electrically isolated from the bulk substrate. In the previous chapter, different ways to control the nanofiber growth have been demonstrated, but in all of the cases, the nanofibers, or the electrodes to which they are connected to (titanium lines), are electrically connected to the substrate (gold film). However, modifications of the substrate designs can be made in order for the grown fibers to be electrically isolated from the bulk substrate.

This chapter shows the design modifications to be made in order to fabricate platform devices for in-situ nanofiber growth, in which the fiber and the electrodes are isolated from the bulk substrate.

4.1 GOLD STRUCTURES ON SiO_2

As shown in section 3.2.2, by depositing p6P molecules on a gold film substrate containing titanium gratings, nanofibers are grown on the titanium lines, even though nanofiber growth is not observed on plane titanium films. Based on these results, it would be expected that the organic nanostructures could also grow on a grating of gold lines, since nanofibers are already formed on planar gold films. By fabricating the gold grating on an insulating material, the resulting p6P nanostructures would be electrically isolated from the silicon bulk substrate, as well the electrodes, which are the gold lines. In this way the nanofibers could be investigated electrically. Figure 24 shows the cross-sectional and top view of such a design.

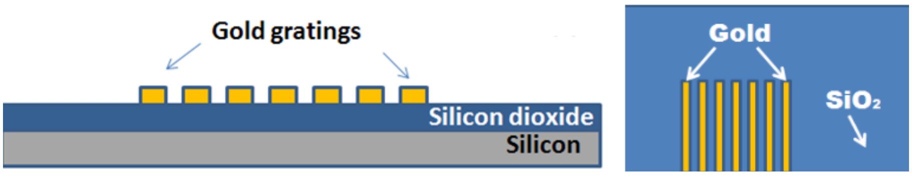

Figure 24: Cross-sectional view (left side) and top view (right side) of the gold gratings on silicon dioxide.

In order to electrically connect the gold lines to a feasible characterization set-up, inter-digitated arrays of gold electrodes forming a grating and connected to larger contact pads were fabricated on silicon dioxide (SiO_2).

4.1.1 EXPERIMENTAL

The samples were prepared by electron beam lithography (EBL) using a Raith ELPHY Quantum lithography attachment on a Hitachi S-4800 scanning electron microscope (SEM), gold deposition by e-beam evaporation and lift-off. The nanofiber growth was performed by vapor deposition of p6P molecules (thickness of 5 nm) onto heated substrates (175°C) under high vacuum conditions (~ 10^{-8} mbar). The nominal thickness and deposition rate (~ 0.1 Å/s) was monitored by a water-cooled quartz microbalance. The images and data for the nanostructures dimensions of the as-grown nanofibers were obtained by SEM and AFM.

Electrical characterization was performed using a custom-built, LabVIEW-controlled measurement setup, where the voltage was controlled by a 16-bit National Instruments DAQ card, which also sampled the current measured by a Stanford Research SR 570 current amplifier.

4.1.2 RESULTS AND DISCUSSION

p6P molecules were deposited on the substrates and organic nanostructures were successfully formed on the gratings and only there, as shown on Figure 25. It is interesting to notice that the gold lines "break" the nanofibers, since they are much longer when growing on the larger gold surfaces. The gold lines reduce the molecules degree of freedom significantly, and their diffusion is hindered, resulting in short nanostructures. In the next chapter, a systematic investigation of the gold line width influence on the resulting fibers morphologies will be presented.

Electrical measurements were made by applying a voltage between the electrodes and measuring the resulting current. The current density (J) was found by dividing the measured current by the total nanostructures cross-sectional area, calculated from the nanostructures dimensions given by AFM (height h) and SEM (width w). The total nanostructure cross-sectional area A_t is found as sum of the cross-sectional area of each fiber (considered to have a semi-circle shape) multiplied by the number of gaps this structure bridges:

$$A_t = \sum_x \frac{\pi h_x w_x N_x}{4}$$

where h_x is the nanostructures height, w_x is the nanostructure width, and N_x corresponds to the number of gaps bridged by this nanostructure.

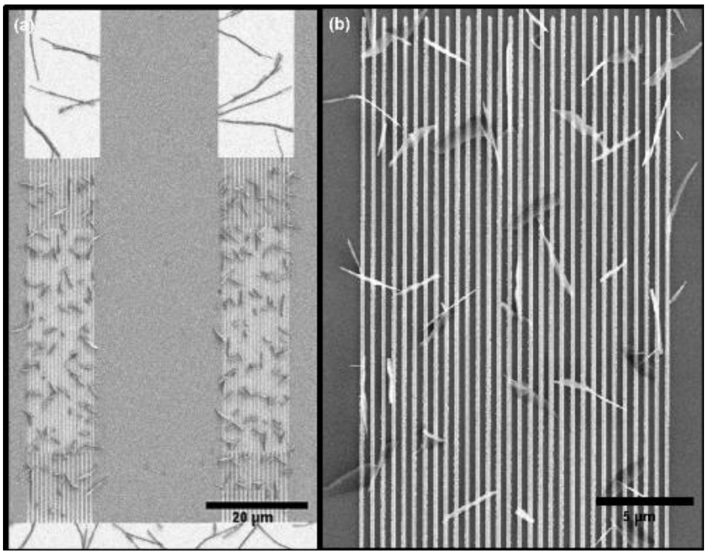

Figure 25: SEM images of gold gratings fabricated on SiO2 after p6P deposition. (a) shows the gratings connected to the larger contact pads and (b) is a higher magnification image of the gold grating, showing the nanostructures grown on the grating.

A typical result of such a two-point measurement is shown in Figure 26 and demonstrates a non-ohmic behavior. The electrical transport properties of individual fibers have previously been studied using a different sample preparation technique [50]: The nanofibers were initially grown on muscovite mica, then transferred to a target platform by drop casting of a nanofiber solution, and finally top contacts were fabricated by a special shadow mask technique employing small silicon wires as local shadow masks. Figure 26b shows a typical J-V characteristic of a single transferred p6P nanofiber with gold top contacts [50]. The two curves in Figure 26a and b exhibit a similar functional form, however, with very different voltage and current density ranges. The individual fiber with top contacts reaches a current density of around 400 mA/cm^2 at an applied voltage of around 3 V, while the in-situ grown structures reach a current density of around 2.5 mA/cm^2 (which is 180 times lower than the transferred fiber) for a applied voltage of 50 V. The current density for the in-situ grown structures has been determined by dividing the measured current with the sum of cross-sectional areas of all nanostructures that bridged the electrodes as described previously. A possible explanation for the large difference between the two cases could be that the total cross-sectional nanofiber area used in the calculation of the current density in the in-situ grown structures overestimates the actual area carrying the current, which could be much lower if only a few structures are carrying the majority of the current due to different contact barriers. Also, it is expected that bottom contacts give rise to larger contact resistances than top contacts do, and the electrical characteristics shown in Figure 26a could therefore be dominated by contact effects. However, the curves present the same parabolic shape for both cases.

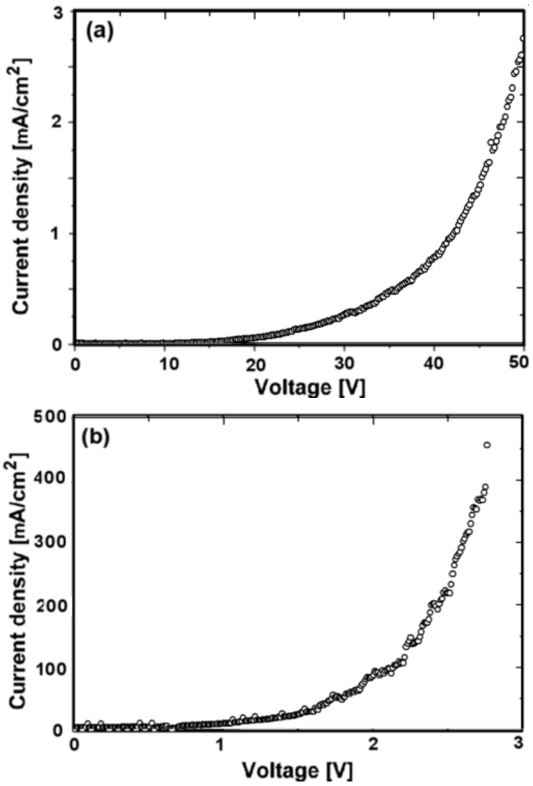

Figure 26: Typical J-V curves of p6P nanofiber devices containing (a) in-situ grown fibers on a gold grating and (b) transferred single nanofiber.

Due to the relatively low conductivity of such organic materials, the electrical transport often occurs in the space-charge limited (SCL) regime [51]. In this case, the maximum current density J is given by the Mott-Gurney law [52]:

$$J = \frac{9\varepsilon_r \varepsilon_0 \mu V^2}{8L^3}$$

where L is the device length, the charge carrier mobility μ is assumed to be a constant, and the relative dielectric constant ε_r is estimated to be 1.9 for the nanofibers [22]. It should be noticed that the Mott-Gurney law provides an upper limit to the current density that can flow in a single carrier device. Any additional effects such as carrier traps or interface barriers will only decrease the current density below this value. Therefore, only the lower boundary of the carrier mobility can be extracted from the Mott-Gurney law [51]. The value for the in-situ grown structures on the gold grating is $2x10^{-5}$ cm^2/Vs, while the value for the transferred fiber is $2x10^{-1}$ cm^2/Vs. It is expected that the electrical characteristics for the samples are different for the transferred fiber and for the in-situ grown structures, since the morphology for both structures are different and since the contact resistance is presumably higher in the bottom-contact structures. However, this large discrepancy can also partly be explained by the problem of determining how many of the fibers grown on the gold grating are actually carrying a current.

By designing a growth substrate with a smaller gold surface area and therefore fewer nanofibers bridging between the electrodes, more detailed investigations of the electrical transport properties become possible. For example, a device platform containing only two gold lines (electrodes) will have fewer fibers bridging, giving more precise results. By reducing the number of electrodes to a pair, these will act as drain and source electrodes in a transistor platform. The silicon dioxide underlayer can act as the gate dielectric and the gate electrode can be fabricated by etching a window into the silicon dioxide in a bottom-gate configuration. For a top-gate configuration, a dielectric (for example PMMA) can be deposited on the fibers and electrodes, and a gate electrode can be deposited on top of the dielectric by nano-stenciling. These two devices were implemented and the results are discussed in the next chapter.

If the design contains 4 electrodes individually connected, fibers grown across the 4 electrodes can be characterized in a 4-point measurement set-up, in order to determine the nanofibers resistance. This device was also implemented and is discussed in chapter 5.

The grating configuration would be useful in platforms where light-emission should be observed. More details will be discussed in chapter 5.

4.2 CHAPTER SUMMARY

This chapter describes design variations for the substrates described on chapter 3, in order to make substrates where electrical characterization becomes possible. The first modification consisted of a gold grating fabricated on silicon dioxide, which is an electrical insulator. The grating has lines connected to two larger bonding pads, making it possible to perform electrical measurements. Organic nanofibers are grown on the gratings, across the lines, and an electrical current is measured by applying a voltage between the bonding pads. However, due to the large number of fibers grown on the grating, it is not so precise to determine electrical characteristics. An alternative is to fabricate only one pair of lines, which would act as electrodes. A further development of this method is presented in the next chapter.

CHAPTER 5

DEVICE CHARACTERIZATION

In the previous chapters, it was demonstrated how the nanofiber in-situ growth on gold surfaces can be controlled by structuring the substrate and how the substrate can be designed to achieve electrical connection for the grown nanofibers. Based on these results, different device platforms for in-situ growth of p6P nanostructures were designed and fabricated: organic field-effect transistors, platforms for 4-point characterization and platforms for light-emitting devices. After p6P deposition, different types of organic nanostructures were formed on the different platforms. The devices design, fabrication and characterization are presented in this chapter.

5.1 ORGANIC FIELD-EFFECT TRANSISTORS

Organic field-effect transistors (OFETs) constitute a promising technology, since they are cheap to fabricate and open the possibility to develop flexible devices. In addition, these devices can be used as platforms for characterizing organic semiconductors and in particular, their transport properties. A typical OFET is composed of three components [53]: an organic semiconductor; a dielectric insulating layer; and three electrodes terminals (source, drain and gate). The current flows through the semiconductor from the source electrode to the drain electrode. The potential difference between the gate and the source controls the current intensity flowing through the semiconductor. This voltage (applied to the gate) induces charges on the interface between dielectric and semiconductor, facilitating the current flow.

For device operation, a voltage is typically applied to the drain (V_D) and gate (V_G) electrodes, while the source electrode is grounded (V_S=0). The source is the electrode from where the charges (electrons or holes) are injected. The charge injection depends if the source is more positive than the gate (hole injection) or more negative (electron injection).

In our devices, the source and drain electrodes are made of gold, whose large work function promotes hole injection [54]. The organic semiconductor consists of p6P nanostructures, grown in-situ on the gold electrodes and bridging the channel gap. This configuration results in a Mott-

Schottky energy scheme as shown in Figure 27 (zero bias). The diagram is a simplified configuration, assuming that there are no interface dipoles.

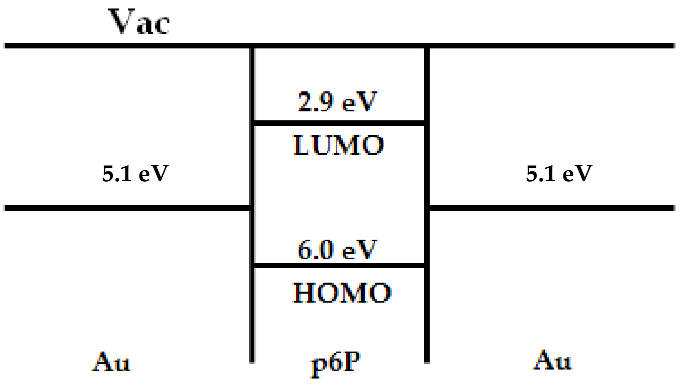

Figure 27: Simplified Mott-Schottky energy schemes at zero bias.

By creating an electrical field (applying a voltage on the drain or gate electrodes), holes can be injected from the Au electrode to the highest occupied molecular orbital (HOMO) while electrons would be injected into the level of the lowest unoccupied molecular orbital (LUMO). Figure 28(a) and (b) are energy schemes for zero drain voltage and negative (a) or positive (b) gate voltages. The energy schemes do not consider the possible interface dipoles or traps between the p6P nanostructure and the gold electrode, which can also affect the device operation.

By applying a negative gate voltage, the energy bands are shifted up and the HOMO level is at the electrode energy level, where holes start to inject. However, by applying a positive gate voltage (b), the energy levels are shifted down and the LUMO level approaches the electrode energy levels, where electrons injection starts. The voltage applied to the drain electrode also plays a role on the energy schemes, as can be seen from Figure 28 (c) and (d). On Figure 28 (c), a negative voltage is applied to the drain electrode, which shifts the energy bands for the drain electrode up. This favors holes injection from the source to the drain electrode. In the other hand, if a positive voltage is applied to the drain (Figure 28d), the energy levels for the drain are shifted down (however there is not electron injection from the source), and holes are injected from the drain. In other words, a negative drain voltage results in a negative current while a positive drain voltage results in a positive current. The negative gate voltage benefits the holes injection into the semiconductor.

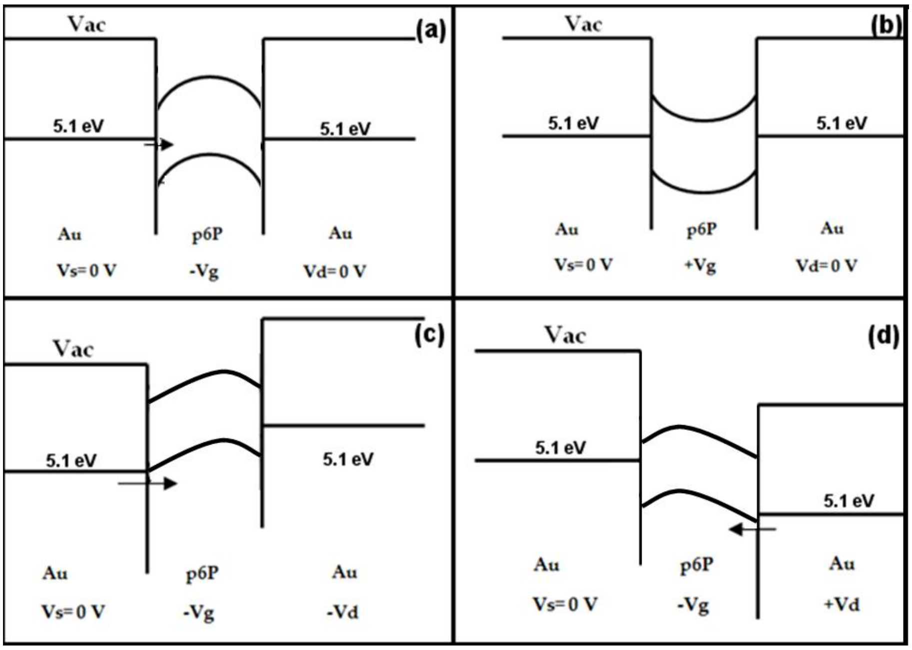

Figure 28: Simplified Mott-Schottky energy schemes at different bias. See text for more details.

There are different device configurations regarding the position of contacts and gate to the semiconductor (Figure 29). Since in the devices presented here, the organic semiconductor nanostructures are grown in-situ on the source and drain electrodes, only the configurations with bottom contacts (electrodes placed under the semiconductor and therefore are located closer to the substrate than the semiconductor) are feasible. The configurations used in the devices presented in this thesis are: (i) bottom-contact/bottom-gate where the gate dielectric is closer to the substrate and the source and drain electrodes are in contact with the gate dielectric (Figure 29a); (ii) bottom-contact/top-gate, where the gate dielectric is located on top of the semiconductor (Figure 29b)

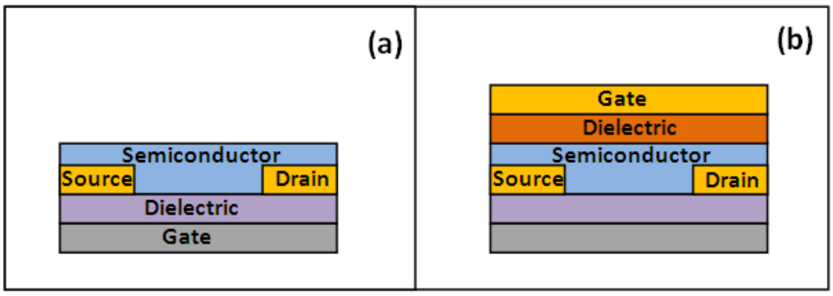

Figure 29: Transistor configurations for in-situ grown semiconductor: (a) bottom-contact/bottom-gate and (b) bottom-contact/top-gate

Silicon dioxide was chosen as the gate dielectric for the bottom-gate configuration, due to its stable dielectric characteristics, the good interface between the bulk substrate (silicon) and the dielectric (silicon dioxide), easy fabrication and the well-known processes regarding etching. For the top-gate configuration, the chosen dielectric was PMMA, since it can be easily deposited by spin-coating over the substrate containing the organic semiconductor without affecting its electrical and optical properties.

5.1.1 BOTTOM-GATE FIELD-EFFECT TRANSISTOR

These devices consist of a pair of gold electrodes with different widths *w* (separated by a small gap *g*) fabricated on silicon dioxide on a highly-doped silicon substrate (see Figure 30a). These electrodes act as source and drain electrodes in an OFET, while the gate electrode is made by etching a window in the oxide all the way to the highly-doped silicon surface and depositing gold on it in order to achieve electrical contact (the gate electrode is the highly doped silicon).

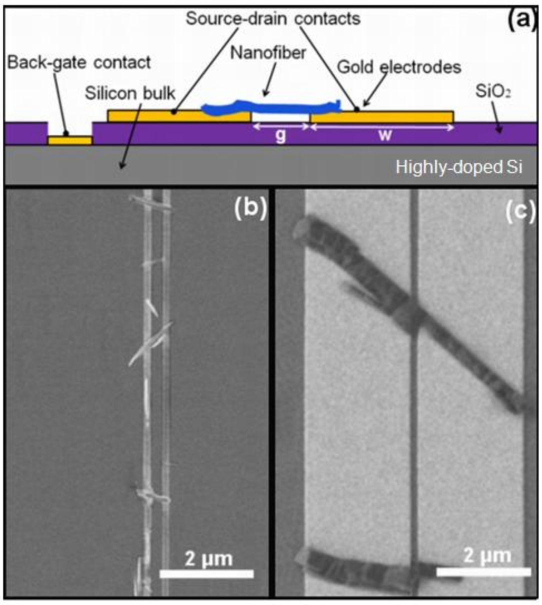

Figure 30: (a) Schematic drawing of the device platform. (b) and (c) SEM images of gold electrodes with g=200 nm and w=150 nm (b) and 2.4 μm (c) after p6P deposition.

Upon deposition of p6P molecules, elongated organic nanostructures are formed on the gold surfaces, in most cases bridging the gaps, thereby establishing electrical connection [55]. The fibers are formed only on the gold surface, since the p6P molecules does not form fibers on silicon dioxide. Instead, the molecules form thin p6P films of standing up molecules, as shown in Figure 31.

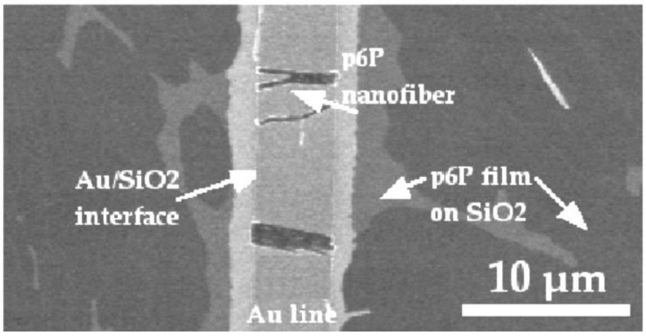

Figure 31: p6P deposited on gold on SiO2

5.1.1.1 EXPERIMENTAL

The device platform is patterned in a mix-and-match process, where large connecting electrodes are first fabricated on 100 nm silicon dioxide on highly-doped silicon by optical lithography, metal deposition (5 nm Ti/30 nm Au), and lift-off. A window (gate) is defined by an extra photolithography step and the silicon dioxide is etched through this window until the silicon substrate is reached, followed by metal deposition (5nmTi/30nm Au) and lift-off. Nanoscale drain and source gold electrodes, partly overlapping the previously fabricated connecting electrodes, are then fabricated by e-beam lithography (EBL), gold deposition and lift-off. The electrode pattern is written by EBL at an acceleration voltage of 30 keV in 150 nm of PMMA resist. After exposure, the pattern is developed by immersion in a 3:1 IPA:MIBK solution, followed by metal deposition of (2 nm Ti/30 nm Au) and lift-off. Finally, the substrates are cleaned in a mild oxygen plasma to remove any organic residues, and the substrates are then ready for nanofiber growth.

Organic elongated p6P nanostructures are grown on the nano-structured gold electrodes by physical vapor deposition of p6P molecules at a rate of 0.1 Å/s from a Knudsen cell. The nominal p6P thickness is 20 nm as measured by a cooled quartz microbalance. During deposition, the substrate is heated to 185^{0}C and the deposition is performed under high vacuum conditions (10^{-9} mbar).

The electrical characterization is made using a custom-built, LabVIEW-controlled measurement setup, where the voltage is controlled by a

16-bit National Instruments DAQ card, which also samples the current measured by a Stanford Research SR 570 current amplifier. The electrodes and nanofibers dimensions are characterized by scanning electron microscopy (SEM) and atomic force microscopy (AFM) operated in tapping mode to avoid damage to the nanofibers.

5.1.1.2 RESULTS AND DISCUSSION

In order to investigate how the electrode design influences the resulting nanostructures, pairs of drain and source gold electrodes were fabricated with the separation gap *g* varying from 150 nm to 1 μm and the electrode width *w* between 150 nm and 2.4 μm; see Figure 30a. The electrodes length is fixed to 15 μm. Figure 30b and c shows SEM images of nanostructures grown on electrodes with two different widths at a gap of 200 nm.

The AFM images and cross sectional profile of each of the representative p6P structures are shown in Figure 32. In both cases, the p6P nanostructures are bridging the gaps; however, there is a difference in the structures morphology depending on the electrode width. Narrow gold electrodes (Figure 32a) lead to tall and narrow nanostructures (here termed "nanoflakes"). This type of structure is also observed for nanostructures formed on alumina templates without gold coating [44]. Wider electrodes (Figure 32b) lead to fiber-like nanostructures ("nanofibers") more resembling those grown on plane (non-structured) gold surfaces.

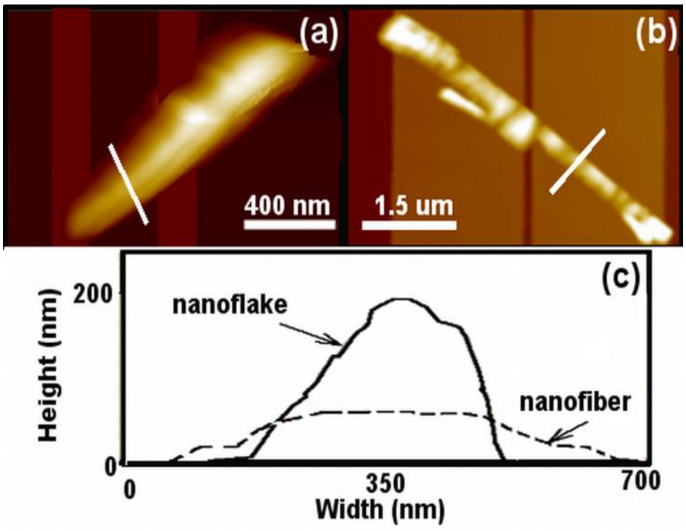

Figure 32: (a) and (b) AFM images of gold electrodes with g=200 nm and (a) w=150 nm (nanoflakes) and (b) 2.4 μm (nanofibers) after p-6P deposition. The cross-sectional profiles of both organic structures are shown in (c).

The molecular orientation in the grown nanostructures was checked by polarization dependent optical measurements. The luminescence output from a p6P molecule is aligned along the long molecular axis. Fluorescence microscopy showed that both kind of structures (nanofibers (Figure 33a-c) and nanoflakes (Figure 33d-f)) emit light polarized approximately perpendicular to the long axis of the nanostructures, which demonstrates that the molecules are oriented in this direction. This indicates that the molecular orientation of both nanofibers and flakes is similar to that known for p6P nanofibres grown on muscovite mica.

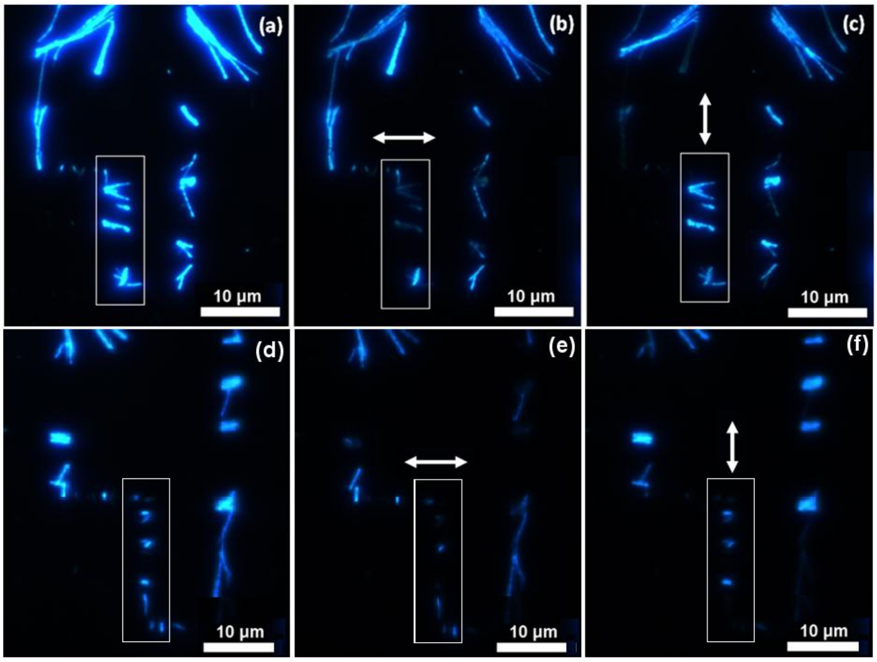

Figure 33: Fluorescence microscopy images of p6P nanofibers grown on gold electrodes; the nanofibers are illuminated with unpolarized light (a) and imaged trough a polarizer (b) and (c). The polarizer direction is parallel (b) and perpendicular (c) to the long nanofiber axis. The same configuration applies to the nanoflakes (d-f).

A systematic investigation of the morphology of the organic nanostructures was made for different electrode widths *w*, by measuring the dimensions (width and height) of the grown nanostructures by SEM and AFM, respectively, and by calculating the aspect ratio, i.e. height to width ratio, as well as the difference between the maximum and minimum heights ($\Delta Z = Zmax - Zmin$) along the long axis of each individual structure. Figure 34a shows how these factors change as a function of the electrode width *w*. The data is based on measurements on about 120 nanostructures. For wide electrodes, the ratio between the average height and the average width of the nanostructures is smaller than for structures grown on narrow electrodes. We propose the following explanation for the phenomenon: On wide electrodes, the surface diffusion area is large, and p6P clusters can aggregate and form long and flat fibers. On narrow electrodes, the surface diffusion area, where clusters are formed, is smaller and the growth is hindered by boundaries. As a consequence, the molecules grow preferentially side by side in the vertical direction since tail to tail growth for rodlike molecules is improbable. The structures grown on wide electrodes exhibit a more jagged morphology, as previously shown for p6P nanofibers grown on gold surfaces. This effect is also shown in Figure 34a, which shows an increase of ΔZ for structures grown on wider electrodes.

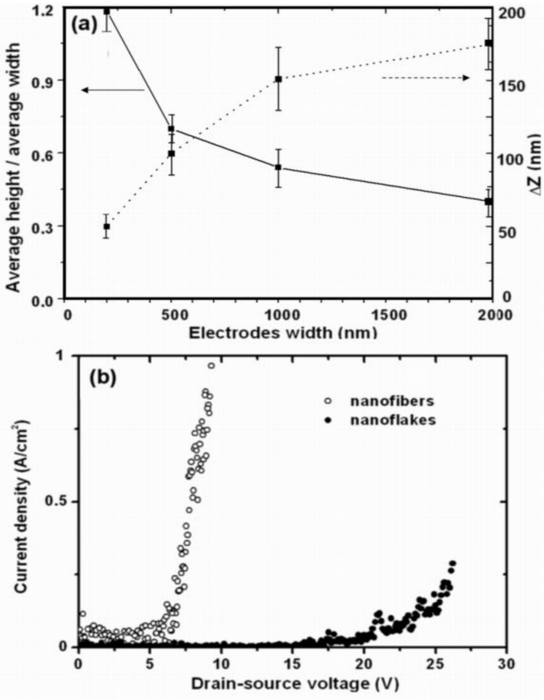

Figure 34: (a) Ratio between average height and average width for the structures grown on electrodes with different widths are plotted as a solid line in the graph. ΔZ factor for the structures grown on electrodes with different widths are plotted as a dashed line in the graph. (b) Electrical characteristics for p-6P nanostructures grown on gold electrodes with *w*=200 nm (nanoflakes) and *w*=2 μm (nanofibers) (Vg=0).

Figure 34b shows electrical measurements made by applying a voltage between the drain-source electrodes and measuring the current flowing through the organic nanofibers/flakes grown on narrow (w=200 nm) and wide (w=2 μm) electrodes, respectively, with zero volts applied to the gate. Measurements prior to p6P deposition were performed to verify that the measured current is not related to any leakage current. The current density values were calculated by dividing the measured current with the total nanofiber/nanoflake cross-sectional area. The curves confirm that it is possible to establish direct electrical connection to organic nanostructures and show a clear difference of the electrical characteristics for the different structures with significantly higher current densities in the nanofibers even at relatively low voltages.

In order for a field-effect transistor to reach saturation, short channel effects should be avoided by having a channel length that is at least 10 times larger than the gate oxide thickness [56-57]. All experiments presented here have been made on substrates with 100 nm oxide, so in order to minimize short-channel effects, the channel length i.e. the gap to be bridged should be increased to 1 μm.

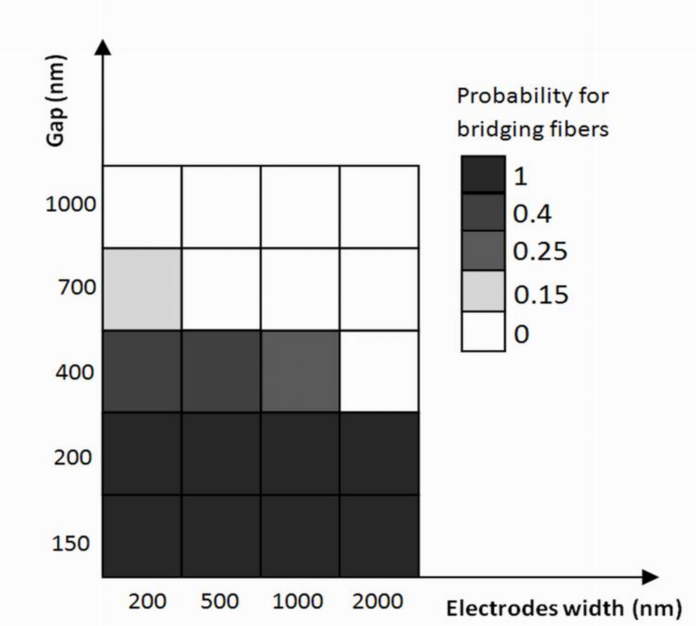

Figure 35: Probability for having at least one bridging p6P structure on a device with varied electrode widths and separation gaps.

The first experiments on platforms with gaps of these dimensions showed that the nanoflakes or nanofibers are not able to bridge such long gaps. In order to determine the maximum gap that the organic structures can bridge, a set of devices with varied electrodes widths *w* and separation gaps *g* were fabricated and investigated. Figure 35 illustrates the probabilities for the organic nanostructures to bridge at different configurations. The data was extracted from around 150 devices, and it shows the probability for the device to have at least one bridging structure. For *g*<200 nm, the probability for bridging structures is 1, but it decreases when g increases and it is 0 for g=1 μm. Therefore, the chosen standard separation gap was 200 nm.

It should be noted that growth parameters such as the substrate temperature during deposition and the nominal p6P thickness have a large influence on the probability for the nanostructures to bridge the gaps. In the present experiments, the substrate temperature was kept constant at 185^{0}C and the nominal thickness was 20 nm. It was observed that there was a high probability for the nanostructures to bridge the gaps under these conditions. At even higher surface temperatures, no nanostructure growth was observed.

More elaborate results of the electrical characterization are shown in Figure 36a, which include output characteristics (I_{DS} vs. V_{DS}) for narrow (w=200 nm) and wide (w=2 μm) electrodes. These were measured by sweeping the drain-source voltage from 0 V to positive voltages, back to negative voltages, and returning and finishing the measurement at 0 V [58]. Each sweep was performed with a constant gate voltage (0 or -10 V). The conductivity of the nanostructures increases when a negative voltage is applied to the gate electrode, showing that both the nanofibers and nanoflakes are p-type semiconductors. However, the minimum drain voltage necessary to have a current flowing is kept approximately constant for positive values in the drain voltage, for the different gate voltages.

In addition, it is seen from Figure 36a that a lower V_{DS} is needed to conduct a current in the nanostructures grown on the wide electrodes (nanofibers) compared to the structures grown on the narrow electrodes (nanoflakes), as was also seen in Figure 34b. We explain this difference in turn-on voltage by the fact that the nanofibers have a larger contact area to the gold electrode surface compared to the nanoflakes, and therefore have a smaller contact resistance. We have not observed any saturation behavior even when the drain-source voltage is swept up to 70 V (at this voltage, the fibers and flakes are destroyed) however, this is as expected since the electrode gap width to oxide thickness ratio is too small. Therefore, the field-effect mobility and the threshold voltage cannot be extracted from the data. The curves sweeping back to 0 V (Figure 36) show higher hysteresis. It means that the current is higher when sweeping from +/- V to zero than when sweeping from zero volts to +/-V. This effect is often observed for organic semiconductors [59] and is most likely due to charge trapping in the dielectric. This discussion will be elaborated in the section 5.1.3.3. It can also be observed that the curves present a degree of symmetry, which suggests that the higher resistance in the device comes from the organic structures themselves, and not from the contact resistance. We attribute this to the fact that the nanofibers are grown directly on the gold electrodes, at high temperature and ultra-high vacuum conditions, which results in a good contact between the p6P structures and the gold electrodes.

The transfer (I_{DS} vs. V_{DS}) curves for the devices containing nanoflakes are shown in Figure 36b. Only the curve for the sweep with negative drain voltage is plotted, because it is difficult to obtain the curve for positive drain voltages, since the onset drain voltage (at different gate voltages) is approximately the same for positive values in the drain voltage.

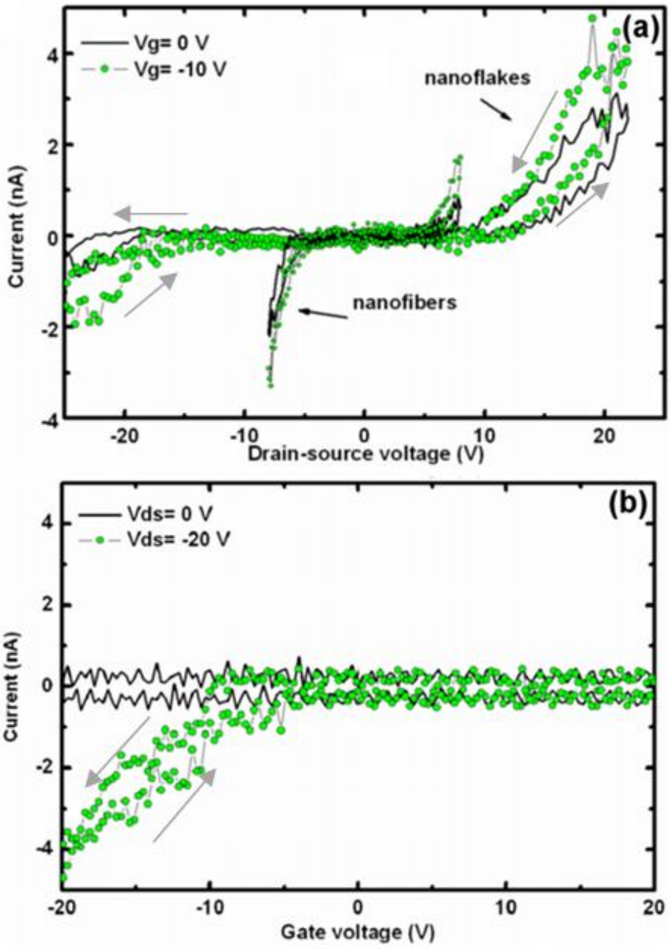

Figure 36: (a) Output curves for devices containing nanoflakes (w=200 nm) and nanofibers (w=2 μm). (b) Transfer curves for the nanoflakes device. The oxide thickness is 100 nm and the drain-source separation gap is 200 nm.

The sweeps were made by sweeping the gate voltage from 0 to 20 V, back to -20 V, returning to 0 V. The drain-source voltage was kept constant at 0 V and -20 V, respectively. These curves confirm that the nanoflakes behave as p-type semiconductors and exhibit an onset voltage of around -10 V.

5.1.2 TOP-GATE FIELD-EFFECT TRANSISTOR

As was shown in the previous section, an applied negative gate voltage increases the conductivity and thereby confirms that holes are the primary charge carriers for the p6P structures. Only the bottom-gate transistor configuration for the grown nanofibers has been demonstrated in the previous section, with highly-doped Si as gate electrode and silicon dioxide as gate dielectric. However, there are some disadvantages for using a bottom-gate configuration. The use of the substrate as a global gate (bottom-gate) implies that all devices are turned on simultaneously, not only the device to be characterized. Also, in the top-gate configuration, the nanofiber is in contact with the gate dielectric, which increases the effect of the gate. The gate dielectric in this case is no longer silicon dioxide, but PMMA. It is expected that the top-gate provides a stronger gate-effect, since it increases the area from which carriers inject [53].

5.1.2.1 EXPERIMENTAL

The device platforms are fabricated as described in the section 5.1.1.1, except that in the platforms described here, the silicon dioxide layer has a thickness of 200 nm. The highly doped silicon substrate also enables bottom-gate measurements, so that the effect of bottom- and top-gate can be directly compared on the same sample.

The p6P nanostructures growth on the previously fabricated platforms is also as described in 5.1.1.1. To complete the top-gate transistors, the platforms are covered with a layer of PMMA, which serves as a top-gate dielectric. A scratch through the PMMA in a third large electrode is made with a micro-manipulation station (see Figure 37). Finally, a top gate electrode (30 nm Au) is deposited by e-beam evaporation over the source-drain contact pair area through a nano-stencil mask [60].

The electrical and morphological characterizations are once more performed as described in the section 5.1.1.1

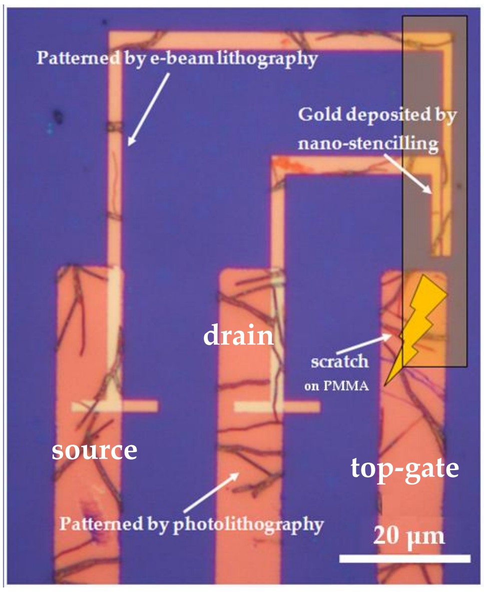

Figure 37: Microscopy image of the sample covered with PMMA. The drawings show the scratch and the gold top electrode.

5.1.2.2 RESULTS AND DISCUSSION

Upon p6P deposition on the substrate containing a pair of gold electrodes, the p6P molecules diffuse on the gold surface and form elongated nanostructures [27], bridging the small gap between the pair of gold electrodes, as shown in the schema in Figure 38a and in the SEM image of the grown nanofibers (Figure 38b). Figure 38c is a cross-sectional view of the device after PMMA and top-gate deposition. A bottom-gate contact is also fabricated on the device, enabling the transistor characterization with both top- and bottom-gate on the same device for direct comparison.

Electrical characterization of the devices was performed and the data shows a very clear enhancement of the current flowing between drain and source when a negative voltage is applied to the top-gate, as can be seen in Figure 39, which shows the output characteristics for a device with the source and drain electrodes width of 1 μm and a gap between the gold electrodes of 200 nm. The drain voltage was kept constant to 0 and -15 V, while the gate voltage was swept from 0 to 15 V, back to -15 V, returning and finishing the measurement at 0 V in both top- and bottom-gate contacts. As can be seen from the figure, the nanofibers again exhibit p-type characteristics, since their conductivity is enhanced when a negative voltage is applied to the gate electrode..

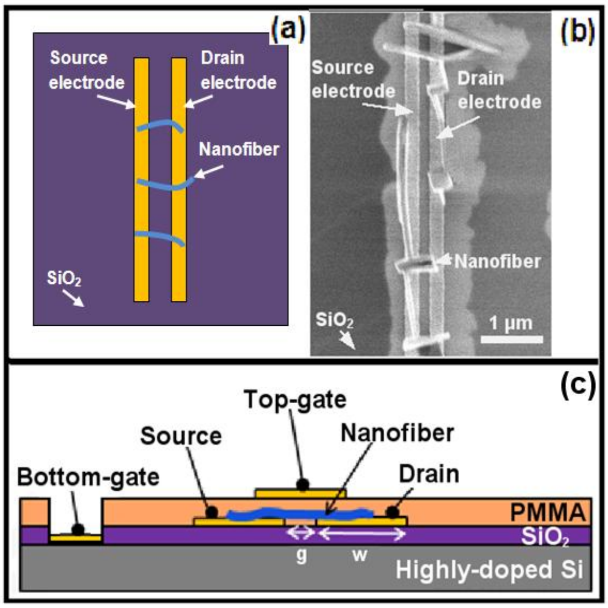

Figure 38: Schema showing a top-view of the grown fibers (a) and a cross-section of the top-gate transistor geometry (b).

Figure 39 also shows that the top-gate has a significantly bigger effect on the nanostructures conductivity than the back-gate. The better top-gate performance is mostly attributed to the area from which the carriers inject, that is larger for the top-gate configuration [61-62]. In the bottom-gate configuration, charges are directly injected into the channel of accumulated charges at the semiconductor-dielectric interface. In the top-gate configuration, charges are injected not only from the edge of the electrode but also from the parts of the electrode that overlap with the gate electrode [63], increasing area from which carriers inject (and the gate effect). One last factor which could influence the device performance is the gate dielectric material. It has been shown that the use of polymeric dielectrics instead of silicon dioxide as gate can improve the device performance due to reduced charge trapping [63], so it would be expected that PMMA (top-gate) would give better device performance than silicon dioxide (bottom-gate).

The curves presented on Figure 39 have a linear behavior for the top gate sweeps. For the linear regime, the charge mobility can be extracted from the gradient of I_{ds} versus V_g at a constant V_{ds}, by the following expression [53]:

$$\mu_{lin} = \frac{\partial I_{ds}}{\partial V_g} \cdot \frac{L}{W C_i V_{ds}}$$

where, L is the channel length (the gap between the source and drain electrodes, here 200 nm), W is the channel width (the sum of the widths of the bridging nanostructures, in this sample 800 nm), C_i is the capacitance per unit area of the gate dielectric (in our case 140 nm thick PMMA, C_i=1.7E-8 F/cm^2), and V_{ds} is the drain voltage.

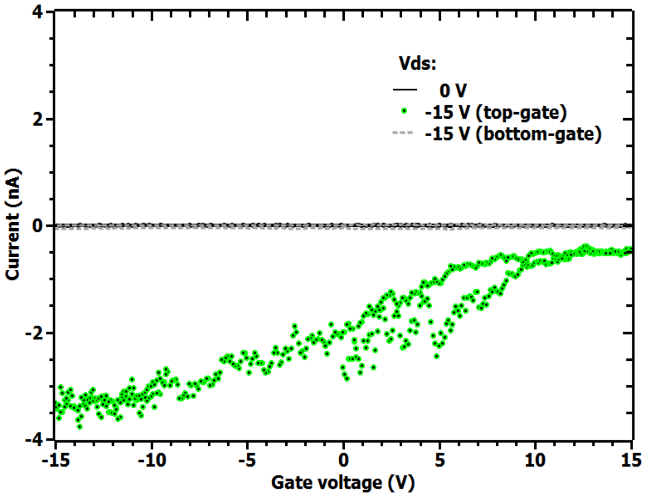

Figure 39: Output characteristics of a sample with both top- and bottom-gate.

By fitting the curve for V_{ds}=-15 V in figure 3, the field effect mobility for the top-gate configuration is given by:

$$\mu_{lin} = 9.3 \times 10^{-5} cm^2/VF$$

5.1.3 GENERAL DISCUSSION OF OFET CHARACTERISTICS

From the different device configurations described in this chapter until now, some characteristics were observed in all samples and should be further discussed. These characteristics are the curves partial symmetry, hysteresis and the absence of the saturation regime.

5.1.3.1 CURVES SYMMETRY

The general behavior for the output curves for the OFETs presented here is partial symmetry. It means that there is a positive electrical current flowing though the organic nanostructure when the voltage applied to the drain is positive, and a negative current flowing when the drain voltage is negative. Our suggestion for explaining this behavior is that the organic nanostructure intrinsic resistance is higher than the resistance between the nanostructure and the contact (see Figure 28c and d). Since the nanostructures are grown in-situ on the gold electrodes, under ultra-high vacuum conditions on a heated substrate, it is expected that the contact resistance is low (since the bounds between the formed nanostructures and the gold surface are strengthen), although a small contact resistance should be found, since the curves are not perfectly symmetric. It can be observed that the nanofibers present more symmetric curves than the nanoflakes, indicating that the contact resistance between the nanofibers and the gold electrode is lower than the nanoflakes contact resistance (due to the contact area, which is larger for the nanofibers).

5.1.3.2 CURVES ABSENCE OF SATURATION

Another common characteristic for all devices is that the curves do not saturate, and therefore, transistor characteristics such as threshold voltage cannot be directly extracted from the curves. This is attributed to the short channel lengths of our devices. Short channel effects result when the drain electrical field penetrates through the channel region and begins to affect the potential barrier between the source and channel regions. Absence of saturation is one of the effects attributed to short channels [64]. In section 5.1.1, it was demonstrated that the maximum channel length for our devices is around 200 nm, since this is the maximum gap for nanostructures bridging the source and drain electrodes in all devices. Transistors with short channel lengths require thin gate dielectrics ($L<10t_{dielectric}$) [56], so the field created by the gate voltage determines the charge distribution in the channel, and not the lateral field of the source and drain electrodes. Otherwise, a limited bulk-current prevents saturation and the gate is not able to determine the on and off states of the transistor [58].

The dielectrics used in our devices (silicon dioxide and PMMA) could not be reduced without a significant leakage current (big enough to influence the device characteristics) start flowing through the dielectric when a certain voltage is applied to the gate electrode. Future work should investigate other possible dielectrics, so that the thickness can be reduced and the short-channel effects prevented.

5.1.3.3 HYSTERESIS

Another characteristic observed in the measurements is hysteresis. In the devices presented here, the hysteresis is always higher and the hysteresis increases for slower sweep rates. Hysteresis effect is often observed for organic semiconductors [59, 65]. Different mechanisms, which would result in hysteresis, were suggested by Egginger [65], and based on these mechanisms, a model for our devices was made. There may be more than one mechanism affecting the hysteresis, but the hysteresis characteristics of our devices indicate that the dominant effect is due to bulk effects of the dielectric [66] (mainly charges trapped in the oxide). These charges could be introduced during device fabrication on the silicon dioxide (e.g. by plasma ashing and e-beam lithography). Since the charges are introduced in the silicon dioxide, which is the dielectric for the bottom-gate devices, and not in the PMMA (top-gate dielectric), it explains the larger hysteresis observed in the bottom-gate devices than in the top-gate devices.

The model is illustrated on Figure 40, which shows typical transfer curves for the devices, with a voltage of -15V applied to the drain electrode. When there is no voltage applied to the gate electrode, the charges in the dielectric are not polarized (1). By applying a positive gate voltage, the charges in the dielectric will be polarized so that the positive charges are located close to the dielectric/semiconductor interface, inhibiting current flowing in a p-type semiconductor (2). By sweeping the gate voltage to negative voltages, the charges reorganize so that the negative charges are located close to the dielectric/semiconductor interface, promoting the flow of holes (3). By sweeping the gate voltage back to zero, the negative charges stay close to the semiconductor, still promoting the flow of holes and causing a higher hysteresis (4).

However, even when there is no voltage applied to the gate electrode, the output curves (drain voltage sweeps) present higher hysteresis. Our suggestion is that the charges flowing through the semiconductor cause the negative charges in the silicon dioxide to approach the dielectric/semiconductor interface. This model is illustrated in Figure 41.

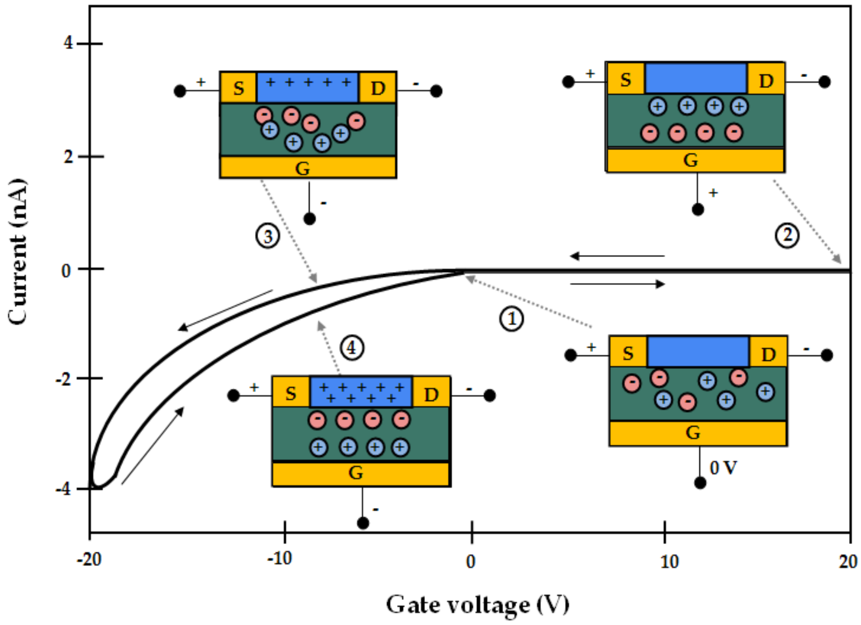

Figure 40: Model for the hysteresis behavior for the gate voltage sweeps.

When there is no voltage applied to the drain electrode (1), the charges in the silicon dioxide are not polarized. By increasing the drain voltage to positive values, an electrical current starts to flow in the semiconductor. The electrical field created by the holes causes the negative charges in the dielectric to approach the interface dielectric/semiconductor (2). When sweeping the drain voltage back to zero, the dielectric remains polarized, so the current flowing in the semiconductor is not only induced by the hole injection from the drain, but also by the charges at the interface (3). When the drain voltage is set to zero, the charges in the dielectric slowly start to move to the initial position, but when the drain voltage is set to negative values, holes are injected from the source electrode, and an electrical current start to flow on the semiconductor again, inducing a similar behavior for the dielectric charges (4).

The evidence for this behavior is shown in Figure 42, which shows consecutive drain-source sweeps for positive voltages without any relaxation time (a). The electrical current increases for each subsequent measurement, since there is not time enough for the dielectric charges to return to the initial position, and therefore, they induce a higher current. If a period of 5 minutes is given between two consecutive measurements (b), the dielectric charges do return to the initial position, and the measurements coincide.

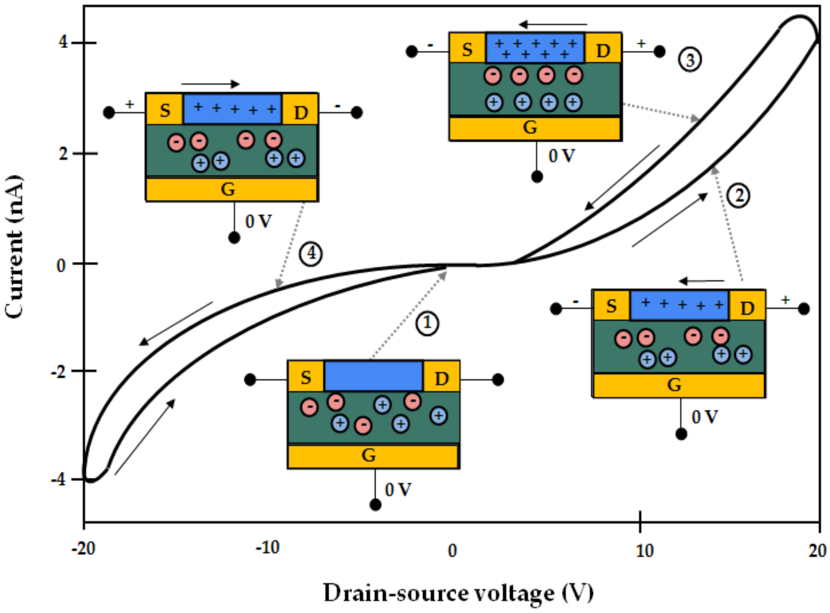

Figure 41: Model for the hysteresis phenomena on the drain-source voltage sweeps.

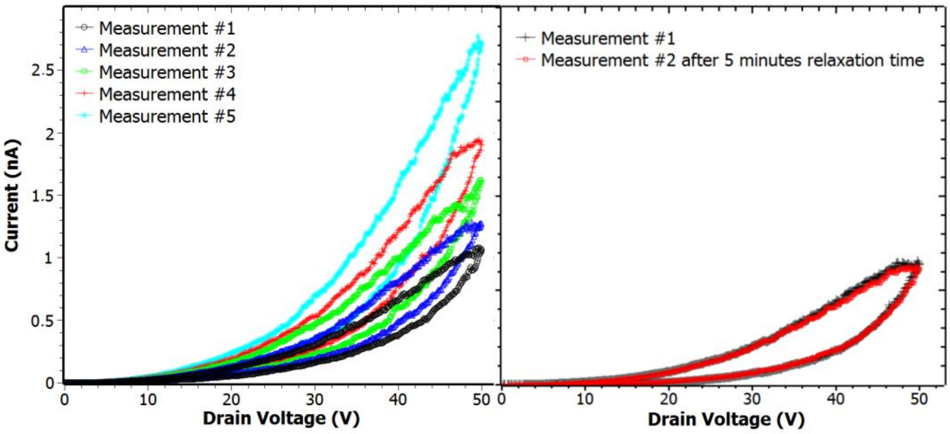

Figure 42: Consecutive drain-source sweeps without relaxation time (a) and with time (b).

5.2 RESISTIVITY MEASUREMENTS (4-POINT)

The OFETs characterization gives us much information about the transport properties for the organic nanofibers. However, in a field-effect transistor configuration, significant energy barriers can exist at the interface between the metal contact and the organic semiconductor [67-68]. In the case of gold contacts and p6P, an injection barrier for holes of ~ 0.9 eV is expected (which results from the difference of energy levels from the HOMO level of p6P and the gold work function), causing the transistor characteristics to be dominated by contact effects, preventing the determination of the nanostructures intrinsic resistance and resistivity.

The four-probe technique is an improved method to determine electrical characteristics of a material [69]. In this configuration, the material to be analyzed is placed across four parallel electrodes. The electrical current flowing between the outermost electrodes is controlled, and the voltage drop between the two inner electrodes is measured. By combining the measured voltage with the current flowing through the material, the bulk resistance of the material can be extracted, eliminating any influence from the contact resistance. In this section, we have demonstrated the p6P nanostructures growth across 4 individually connected gold electrodes, which enables electrical measurements to extract the bulk resistance and intrinsic resistivity. Figure 43 illustrates how such a platform should be designed. The nanofiber is grown across 4 gold lines. An electrical current is applied to the outer lines while the voltage between the inner lines is measured. The inclination of the curve VxI gives the value for the nanofiber resistance.

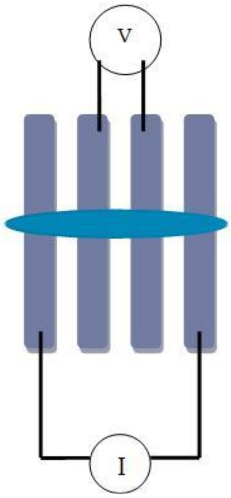

Figure 43: Schema for a 4-point measurement platform.

5.2.1 EXPERIMENTAL

These device platforms are fabricated by the same processes as described in section 5.1.1.1, except by the absence of a gate electrode. The nanofiber growth and morphological characterizations are also similar to the process described in 5.1.1.1. In addition, a thin amorphous p6P film was deposited on one of the platforms for 4-point measurements. The nominal p6P thickness is 30 nm as measured by a cooled quartz microbalance and the substrate is kept at room temperature during deposition.

The electrical characterization is made using a Keithley 2400 digital sourcemeter, which applies the current to the outer terminals while measures the voltages drop between the inner terminals.

5.2.2 RESULTS AND DISCUSSION

The field-effect transistor configuration is useful to determine the transport characteristics of the organic nanostructures. However, intrinsic resistance and resistivity of the nanostructures cannot be extracted from this configuration, since the characteristics can be dominated by contact effects. In order to determine these electrical properties, the nanostructures were grown across 4 individually connected gold electrodes, so as to enable 4-point measurements that avoids contact effects.

Under appropriate deposition conditions (substrate temperature and p6P thickness), the p6P nanostructures are sufficiently long to span 4 gold lines, enabling electrical 4-point characterization. Some of the samples containing these p6P structures are shown in Figure 44, which are SEM images of the grown fibers. We have named the nanostructures as NS1, NS2 and NS3. As can be seen from the images, there are different morphologies for the structures, depending on the electrode design.

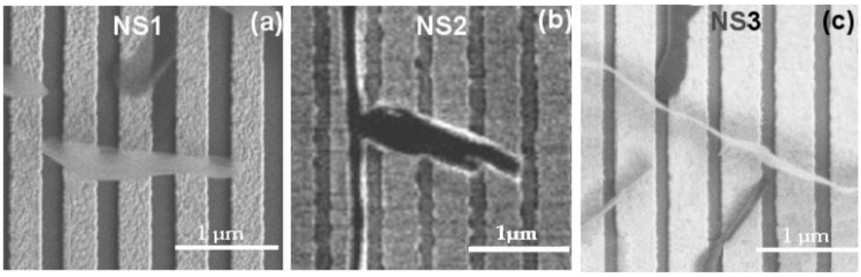

Figure 44: SEM images of gold electrodes containing p6P nanostructures with different morphologies, named NS1, NS2 and NS3 (see text for details).

AFM images of the nanofibers are shown in Figure 45. By comparing these images with the SEM images in Figure 44, the morphologies can be determined in more detail. The line width of the gold electrodes has a strong influence on the nanostructure morphologies, as reported previously [55].

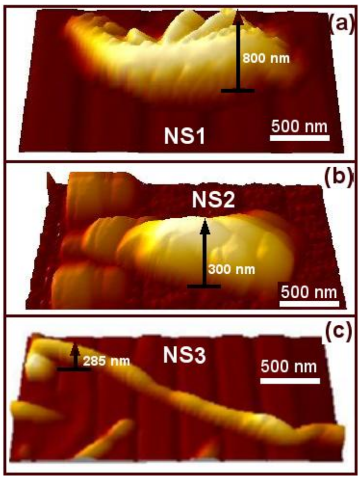

Figure 45: AFM images of the different nanofibers.

For the narrow gold lines, the molecular diffusion is hindered by the gold line boundaries, and the molecules form high and narrow structures, here termed nanoflakes. The nanostructure named NS1 is an example of such a structure. By increasing the gold line width, the nanofiber height is proportionally reduced, as on the structure NS2. All data for the dimensions of these structures are presented in table 1. One should observe that there is an error margin when estimating the nanofibers dimensions. This error margins (s_D) are found by determining the maximum (D_{max}) and the minimum (D_{min}) values for the nanofibers dimensions, and defined as:

$$s_D = \frac{D_{max} - D_{min}}{2}$$

For the electrical characterization, a current is applied between the two outer electrodes (I_{14}) and the voltage drop between the two inner electrodes (V_{23}) is measured. The resistivity of the substrate itself (gold grating) without grown fibers was also measured and found to be around 12 GΩ. This resistance was taken into account in the nanostructures resistance determination as a parallel resistance. The plot for the current I_{14} versus the voltage V_{23} for NS3 is presented on Figure 46. As can be seen, the curve has a linear and ohmic behavior, so the nanostructures intrinsic resistance can be directly extracted from the curves. The intrinsic resistances for the nanostructures are found to be between 1.5 GΩ and 2.7 GΩ (the values are listed in table 1). The intrinsic resistance (17.24 GΩ) and resistivity (30450 Ω.m) of an amorphous p6P thin film deposited on the substrates for 4-points measurements were extracted. It allows us to compare the resistivity of an amorphous p6P film with the resistivity of the crystalline nanostructures.

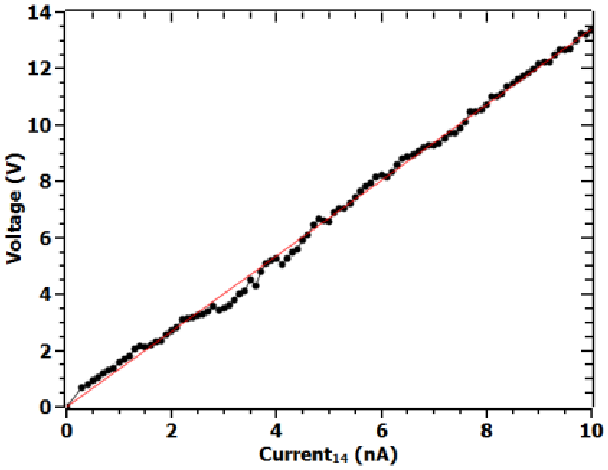

Figure 46: Current versus voltage plots for 4-point measurements.

The nanofiber´s resistivity is given by:

$$\rho = \frac{RA}{l}$$

where R is the fiber resistance, which is found from the electrical measurements, A is the cross-sectional area of the fiber, which can be extracted from AFM and SEM images, and *l* is the nanofiber length to what the measurement is performed (defined as the gap between two subsequent gold lines of the gold grating).

The nanofibers cross-section is calculated by:

$$A = \frac{\pi WH}{4}$$

Assembling all data, the resistivities of the nanofibers are calculated and shown in table 1:

Nanostructure	Resistance (GΩ)	Width (nm)	Height (nm)	Length (nm)	Resistivity ρ (Ω.m)
NS1	2.62 (±0.08)	50 (±30)	800 (±200)	220 (±10)	374 (±244)
NS2	1.51 (±0.01)	300 (±50)	300 (±50)	180 (±20)	594 (±155)
NS3	2.56 (±0.1)	120 (±30)	250 (±50)	140 (±10)	430 (±142)
p6P thin film	17.24 (±4)	15000 (±200)	30 (±2)	200 (±10)	30450 (±7190)

Table 1: Nanostructures properties.

As can be seen from the table, the resistivities for nanostructures are of the same order for NS1, NS2 and NS3, while the value for the amorphous thin film resistivity is much higher (about 65 times) than the resistivity values for the elongated nanostructures. It seems that the p6P structure (nanofiber or thin film) degree of crystallinity plays a very important role on the structures electrical properties. The resistivity for the amorphous p6P film is comparable to the lowest resistivity value for the single crystal pentacene (25000 Ω.m) [70].

5.3 LIGHT-EMITTING DEVICES

The third device platform consists of gold electrodes fabricated on silicon dioxide and connected to source and drain terminals. A back-gate is fabricated on the substrate using the same method as for the bottom-gate field-effect transistors. The objective is to obtain injection of holes and electrons from the source and drain electrodes into the nanofibers. This can result in electron/hole recombination and light-emission.

As it was shown in the section about OFETs, our devices are unipolar, since only holes are injected from the source (or drain) electrode into the nanofiber. Applying a DC voltage to the gate electrode, simultaneous injection of holes and electrons cannot be achieved. It was shown that p6P thin films present electro-luminescence when deposited on a transistor platform and an AC voltage is applied to the gate [71-72] while the source and drain electrodes are biased symmetrically relative to the gate. If both injecting electrodes have high barriers, a DC voltage cannot aid carrier injection at both electrodes simultaneously. If an AC voltage is applied, the barriers for hole (negative gate) and electron (positive gate) injection are reduced, allowing both types of charges to be injected into the semiconductor.

Therefore, light-emission measurements were performed on the transistor platforms presented in section 5.1. However, the nanofibers were too small to be resolved with the available microscope equipment. A new design was made in order to increase the number of fibers and the total area containing nanofibers, so that the luminescence would be visible.

5.3.1 EXPERIMENTAL

The device platform fabrication and nanofiber growth are similar to the process described in section 5.1.1.1.

The light emission experiments were done under vacuum conditions (10^{-4} mbar). Source and drain were symmetrically biased relative to the ground using two Delta Elekronica ES075-2 DC power supplies while a Grundig FG100 function generator in combination with a Falco Systems WMA-300 voltage amplifier biased the gate. Light emission was detected with a Navitar microscope and a Lumenera Infinity 1 camera.

5.3.2 RESULTS AND DISCUSSION

The first attempts were made by using the same devices as presented on section 5.1. However, the area to which the nanofibers are bridging the source and drain electrodes is too small to be resolved by our set-up. In addition, there are only 2 or 3 nanofibers bridging the electrodes, what makes it very difficult to notice any light emission, as can be seen from Figure 47. In this sample, a frequency of 60 kHz for the AC voltage was applied to the gate electrode with an amplitude of 50 V. The source and drain electrodes are grounded.

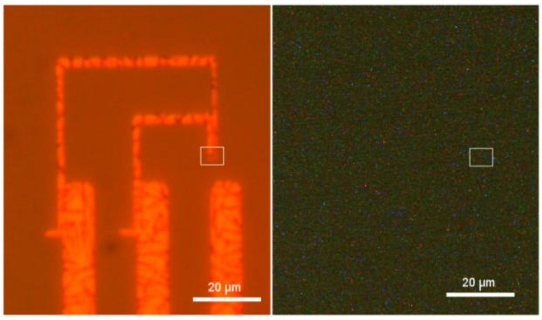

Figure 47: Microscopy image before the measurement (a) and during the measurement (b).

In order to increase the area containing bridging nanofibers, a new design was made, where instead of a single pair of gold electrodes, gold lines placed as a grating and connected to two terminals are patterned as shown on Figure 48, which is a SEM image of the gold structures on silicon dioxide before p6P deposition.

After p6P deposition, nanofibers are formed on the gold gratings, bridging the lines. The sample is placed in a vacuum chamber and an optical microscopy image of the device illuminated with white light was taken and is shown in Figure 49(a). The two electrodes to which the gold lines are connected (source and drain) are symmetrically biased (in this measurement, to 0 V), while an AC voltage is applied to the gate electrode, which resulted in electroluminescence, as can be seen in Figure 49(b) and (c), which are optical microscopy images of the device.

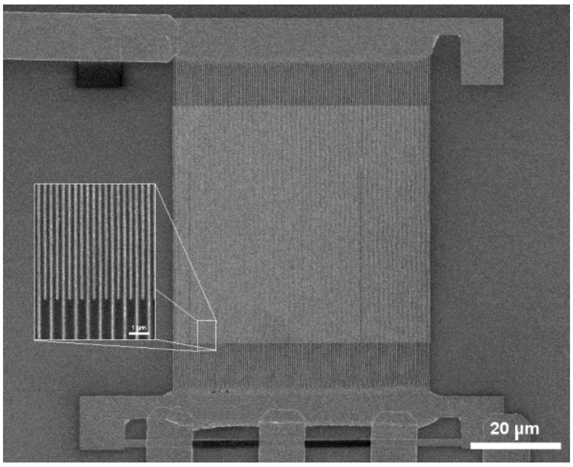

Figure 48: SEM image of the substrate for light-emitting devices before p6P deposition. The scale bar for the inset figure is 1 μm.

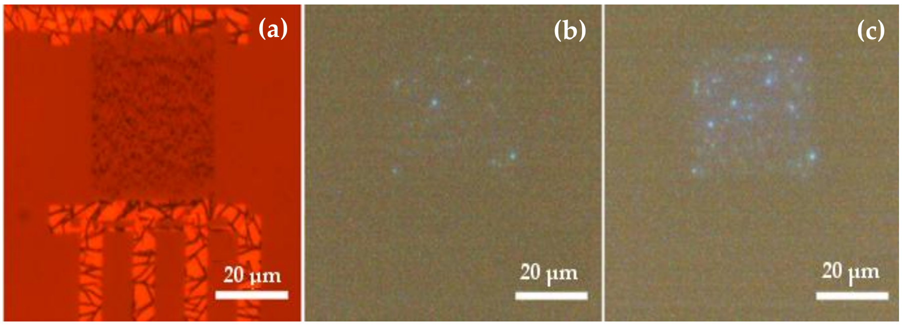

Figure 49: (a) Optical microscopy image of the gold grating illuminated with white light before measurement. (b) and (c) Optical microscopy images of the device when an AC voltage is applied to the gate with amplitude and frequency of 45 V and 40 kHz (b) and 50 V and 100 kHz (c), respectively.

The light intensity is higher in (c) than in (b), and this is due to the different conditions applied to the device in each case. In image (b), the amplitude of the AC voltage applied to the gate is 45 V, while in image (c), the amplitude is 50 V. In addition, the AC frequency during the first image is 40 kHz, while in the second it is 100 kHz. Therefore, it can be concluded that these parameters have a strong influence on the light intensity. The higher intensities for higher frequencies are mostly due to the larger number of cycles causing more recombination events per unit time [72].

As can be seen from the images, not all nanofibers emit light, and some of them present higher light intensity than others. In order to determine which kind of nanofibers have stronger light-emission, SEM and AFM images of the device were obtained and directly compared to the electro-luminescence images, as is shown in Figure 50.

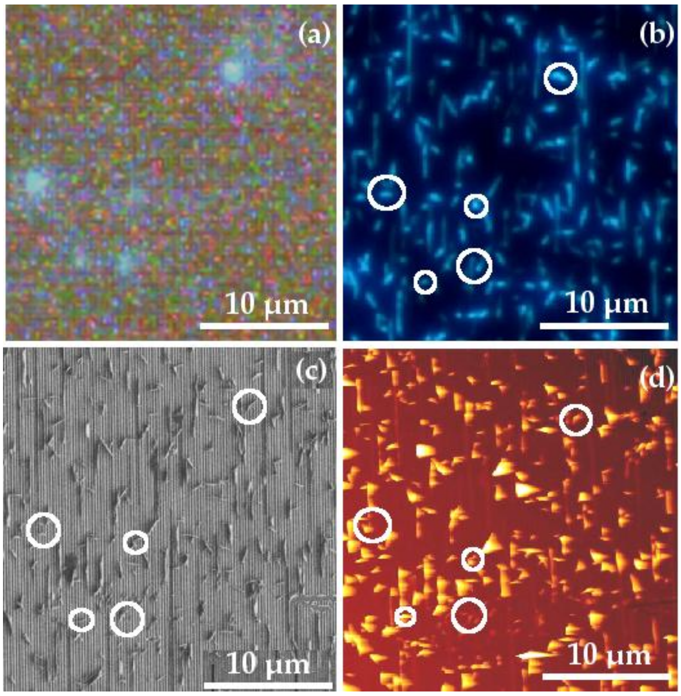

Figure 50: Ligth-emitting device characterized with different techniques. (a) electro-luminescence; (b) fluorescence microscopy; (c) SEM and (d) AFM

The photo-luminescence of the nanostrucures is shown in Figure 50b. All the luminescent structures in the figure present polarized light, indicating that they are crystalline. But not all the structures are electro-luminescent, which indicates that crystallinity alone is not sufficient for observing the effect. The condition for the nanostructure to emit light must be related to another property, such as morphology or the electrical contact between the nanostrucure and the gold electrodes. Figure 50c and d are SEM and AFM images of the nanostructures. As can be seen from the image, the electroluminescent structures are growing perpendicular to the gold lines long-axis. In addition, they show not to be the highest structures on the AFM image, but mostly low.

This morphology (flat fibers), probably gives the structures a better electrical contact to the gold lines, as was discussed previously (low nanofibers and high nanoflakes). With a better electrical contact, more charges can be injected from the gold electrode into the nanofiber, causing a larger number of recombination events, and therefore, higher light intensity.

However, there are more fibers that fulfill the same conditions but do not light up. It might be more effects influencing on the electroluminescence properties of individual nanofibers, which should be investigated on future work.

On OFETs, we have demonstrated that the top-gate configuration is more effective, since the gate effect is enhanced. Therefore, future work should focus on developing OLEDs with top-gate. However, the gate electrode material should be transparent so that the light can be detected.

5.4 CHAPTER SUMMARY

Devices containing in-situ grown nanofibers as active semiconductor layers were presented in this chapter. Different configurations for organic field effect transistors were presented here, with top- or bottom-gate. For all configurations, the nanofibers conductivity is increased when a negative voltage is applied to the gate electrode, showing that the nanofibers are p-type semiconductors. The influence of the device configuration (top- or bottom-gate) and design on the transport properties of in-situ grown organic nanostructures was also investigated and the top-gate configuration is shown to have a stronger effect on the nanostructures conductivity than the bottom-gate.

In addition, we have demonstrated a method to determine the intrinsic electrical properties of p6P nanostructures, in-situ grown on gold electrodes. This method consists of growing the organic structures across four individually connected gold lines, allowing 4-probe measurements to be performed. The nanostructures morphology depends on the gold electrodes dimensions, and narrow electrodes lead to narrow and high structures (nanoflakes), while wide electrodes lead to more flat and wide structures (nanofibers). The resistivities of the structures depend of their degree of crystallinity.

The electroluminescence properties of the in-situ grown nanofibers were also demonstrated by growing the fibers on a transistor platform and applying an AC voltage to the gate electrode. The nanostructures morphology seems to have an influence on the emitted light intensity, but it might be only one of the effects influencing the electroluminescence properties.

CHAPTER 6

LARGE-SCALE FABRICATION BY NANOIMPRINT LITHOGRAPHY

All the devices platforms presented in this thesis require structures and gaps of nanometric sizes, since the nanofibers are grown directed on the small electrodes. Until now we have fabricated the devices by a combination of photolithography and e-beam lithography. The next step was to fabricate the optimized designs at large scale by nanoimprint lithography.

Nanoimprint lithography (NIL) was first demonstrated by Chou [73] and the interest for the technique has increased since then, especially due to the possibility of fast nano-scaled device fabrication over large-area. Nanoimprint lithography combines the speed of optical lithography with the resolution of e-beam lithography. It creates patterns by mechanical deformation of imprint resist and subsequent processing. There are many different types of nanoimprint lithography, but two of them are most important: thermoplastic nanoimprint lithography (where the polymer is cured by a change in temperature) and photo nanoimprint lithography (where the polymer is cured by exposure to UV light). The processes described here are made using photo nanoimprint lithography.

The stamp is fabricated by imprinting a silicon wafer containing the designs (negative structures) on a plate coated with QuickMold™ polymer. The results show that is possible to imprint a pattern containing both large contacts (300 μm x 2 mm) and nano-structures (sizes from 200 nm and gaps from 60 nm), using the same stamp in one step. The imprints are performed with a NanoLithoSolution (NLS) nanoimprint module add-on to a photo-lithography mask aligner and the processes are described in the following sections. The complete process can be found in attachment 2.

Additional samples were fabricated in collaboration with the *Octopus Project* partners by using an *Imprio 100* equipment from *Molecular Imprints*, which is a high-resolution system producing high-quality samples. More details about these samples are presented in section 6.7.

6.1 MOLD FABRICATION

The first step is to fabricate a silicon mold containing the negative of the pattern to be fabricated. Since our devices have both micro- and nano-sized structures, the very first step is to define the microstructures by standard optical lithography on a silicon wafer. The patterns are then etched down to 70 nm depth in an inductively coupled plasma reactive ion etching (ICP-RIE) system from Alcatel (AMS 110), with a mixture of SF_6 and C_4F_8 for 4.5 s. After etching, the resist is removed in acetone and cleaned in oxygen plasma (5 minutes, 200 W).

After definition of the microstructures, the nanostructures are defined on the wafer by e-beam lithography. The steps are shown in Figure 51. First, a layer of 150 nm PMMA A4 is applied to the silicon wafer, followed by alignment and definition of the patterns by e-beam lithography. The wafer is then immersed in a solution of 1:3 MIBK:IPA for 40 seconds and rinsed in IPA for 30 seconds for pattern development. The next step is to etch the silicon (70 nm deep) trough the PMMA mask by ICP-RIE with a mixture of SF_6 and C_4F_8 for 5.5 s. After etching, the PMMA is removed in acetone and cleaned in oxygen plasma (5 minutes, 200 W).

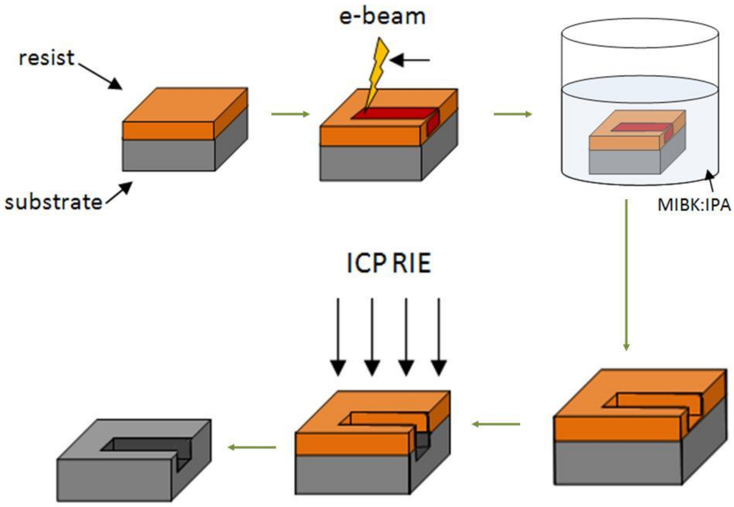

Figure 51: Steps for silicon mold fabrication

The silicon mold is used to fabricate the stamp by imprinting it into a flexible polymer (mold resist), which assumes the mold form and is cured by UV-light. However, imprint is a contact technique, and the main problem with such a technique is the release problems caused due to sticking of the substrate and the stamp. Therefore, an anti-sticking coating has to be applied on the substrate to avoid these problems.

6.2 ANTI-STICK COATING

The anti-stick coating is applied on the silicon wafer surface following a recipe suggested by Beck [74]. Silanol groups have to be formed on the silicon surface, requiring an oxygen plasma step (5 minutes, 200 W). A solution of 0.5 surfactant (1ml F_{13}-TCS to 200 ml heptane) is prepared. The wafer is immersed in the solution for 1 hour and rinsed with heptane afterwards. In order to strengthen the bonds, the wafer is baked at 180^{0}C for 2 minutes.

This process creates a monolayer on the silicon surface, where the silanol groups on the silicon surface form covalent bonds with the molecules headgrup, while the fluorinated alkylgroup forms assembled tail groups with the anti-sticking properties, as can be seen on Figure 52.

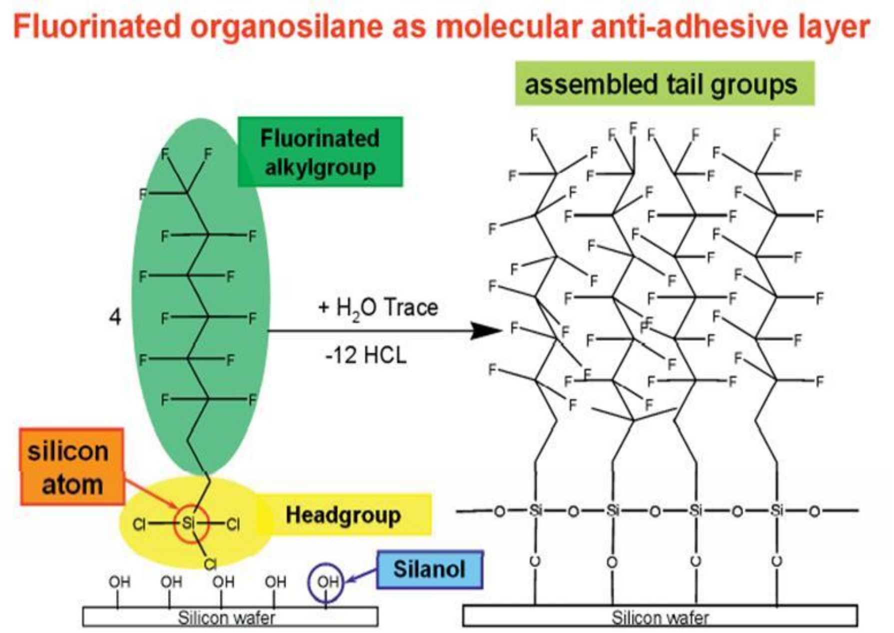

Figure 52: Anti-sticking tail groups on silicon [75].

6.3 STAMP FABRICATION

After the silicon mold fabrication containing both large and small structures, the next step is to fabricate the stamp. It is made by starting with a clean (piranha solution) glass or quartz plate, which is coated with a layer of AR-ULP (underlayer lift-off resist) which promotes adhesion between the quartz plate and the QuickMold™ polymer, baking it for 120 s at 200⁰C and applying a layer of AR-UVM (the mold resist: assumes the form of the silicon mold) on top of it. The plate is imprinted on the previous made silicon mold at pressure of 20 psi, and cured with UV-light (intensity: 8 mW/cm^2) for 500 seconds. The wafer is then released. The steps are shown in Figure 53. The resulting stamp contains the patterns with the same dimensions as the silicon mold, and a height of 70 nm.

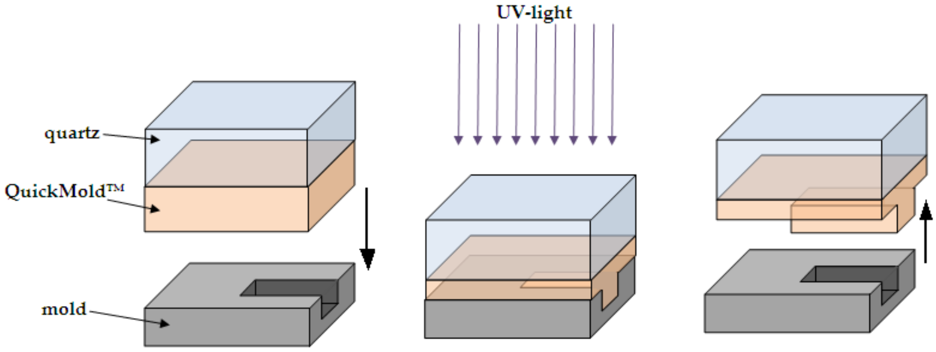

Figure 53: Steps for stamp fabrication

The anti-stick layer has to be applied on the stamp, and it is made in the same way as described on the previous section. The stamp is then ready for imprinting.

6.4 IMPRINT AND FABRICATION

The general process for photo NIL is shown in Figure 54. The stamp contains the patterns to be defined on the substrate. The stamp is pressed into the polymeric material (resist) previously deposited on the substrate (Figure 54a). When the stamp is filled with polymer, it is cured by UV light through the stamp, obtaining the stamps shape (Figure 54b). A residual layer of resist is left and has to be removed (Figure 54c).

The wafer to be imprinted is coated with a layer of AR-ULP (underlayer lift-off resist) which facilitates the lift-off process, baked for 90 s at

200^0C and coated with a layer of AR-UV (the UV sensitive resist) on top of it. The wafer is imprinted with the previously made stamp at pressure of 28 psi, and cured with UV-light (intensity: 8 mW/cm^2) for 250 seconds. The wafer is then released. As the resist thickness is around 150 nm and the stamp structures height around 70 nm, the pattern is not imprinted trough the whole resist layer. The residual layer of AR-UV and the lift-off underlayer (AR-ULP) has to be etched. The residual layer is etched on the ICP-RIE with a gas mixture of O_2 and SF_6 for 1 minute. The underlayer (AR-ULP) is etched selectively with O_2 for 3 minutes, without further etching on the AR-UV layer, increasing the aspect ratio and facilitating the lift-off process.

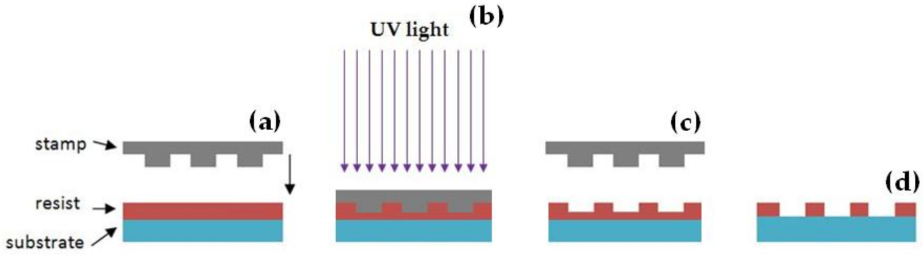

Figure 54: Imprint process (see text for details).

After the residual layer and underlayer etching, metal can be deposited on the substrate, and lifted-off, as is shown in Figure 55.

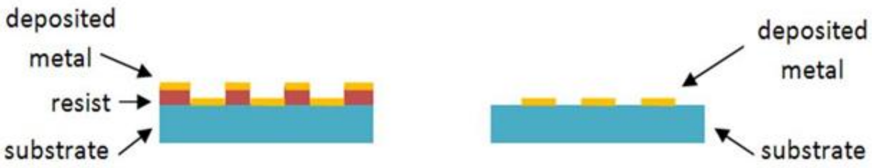

Figure 55: Metal deposition and lift-off.

For the device platforms developed on this thesis, 2 nm of Ti and 30 nm of Au were deposited by e-beam evaporation and the resist was lifted-off by immersing the wafer on an Acetone solution for 5 minutes under ultrasonic agitation.

6.5 RESULTS

The substrate wafer contains gold structures with both micro- and nano-dimensions, fabricated in one single imprint step on a whole wafer (see Figure 56). If the silicon substrate contains a layer of silicon dioxide, the gold structures are fabricated on the silicon dioxide layer, as it was done for the previous presented devices. These devices can therefore be produced at large-scale.

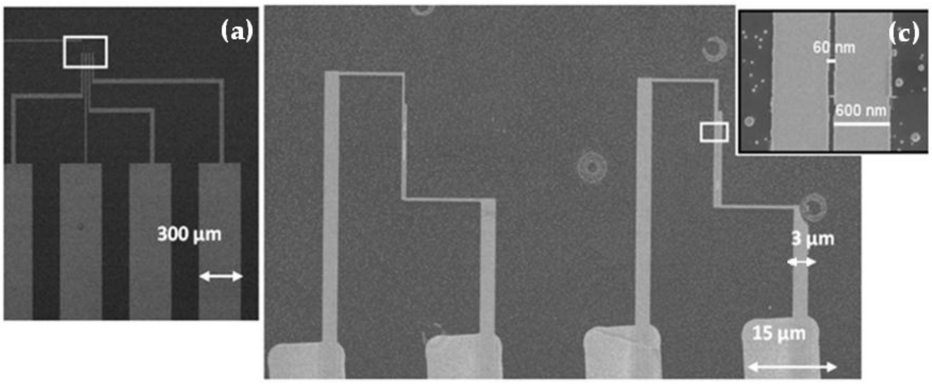

Figure 56: SEM images of gold structures on silicon fabricated by NIL, gold deposition and lift-off. (a) Low magnification image showing the large contacts. (b) Zoom into the white rectangle in (a). (c) Zoom into the rectangle shown in (b).

As can be seen on Figure 57, different designs can be fabricated by NIL, allowing devices variations. Figure 57a and b shows designs for OFETs and Figure 57c shows designs for 4-point measurements platforms.

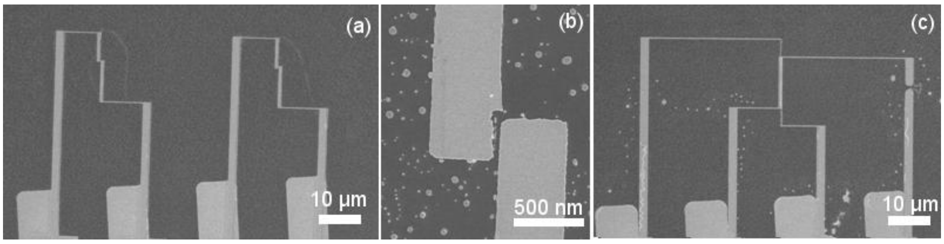

Figure 57: Different designs fabricated by NIL. (a) and (b) platforms for OFETs. (c) platform for 4-point measurements.

6.6 NANOFIBER GROWTH

After fabrication of device platforms by nano-imprint lithography, the nanofiber growth can be performed by using the same method as for the samples fabricated by e-beam lithography, as can be seen in Figure 58, which is an SEM image of the gold electrodes fabricated by NIL after p6P deposition.

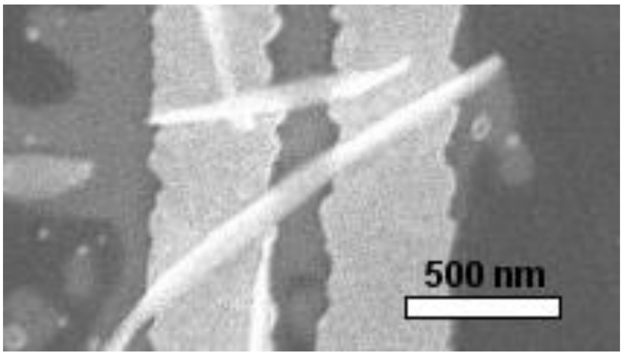

Figure 58: SEM image of the gold electrodes fabricated by NIL after p6P deposition.

6.7 SAMPLES FROM *OCTOPUS PROJECT*

In addition to the samples fabricated in the NanoSYD cleanroom, some device platforms were fabricated in collaboration with the Danish Technological Institute (DTI) and their equipment located at DTU Danchip, which are both partners in the Innovation consortium Octopus (whose purpose is to further develop the use of nano-imprint lithography in Denmark, and is the sponsor of this Ph.D. project).

These samples were fabricated using an *Imprio 100* tool. This tool uses Step and Flash Imprint Lithography (S-FIL), which instead of depositing the UV sensitive polymer prior to the process it is deposited immediately before the stamp contact. This allows the use of low viscosity polymers, requiring a lower imprint pressure [76]. The stamp is fabricated on a quartz template using e-beam lithography.

Figure 59 shows SEM images of these device platforms. The patterns consist of 5 nm Ti/ 40 nm Au on 200 nm silicon dioxide. Figure 59a shows the overview of the sample, with large electrodes leading to nano-scaled electrodes, as shown in Figure 59b (4-gold lines individually connected) and c (a pair of gold electrodes).

After p6P deposition, nanostructures are formed on the gold areas, bridging the small gaps between the gold lines, as shown in Figure 59b, enabling electrical characterization. The curves show that the devices fabricated by NIL have similar electrical properties as the ones fabricated by EBL, as can be seen in Figure 60, which shows the transfer curve for Vg= 0 V.

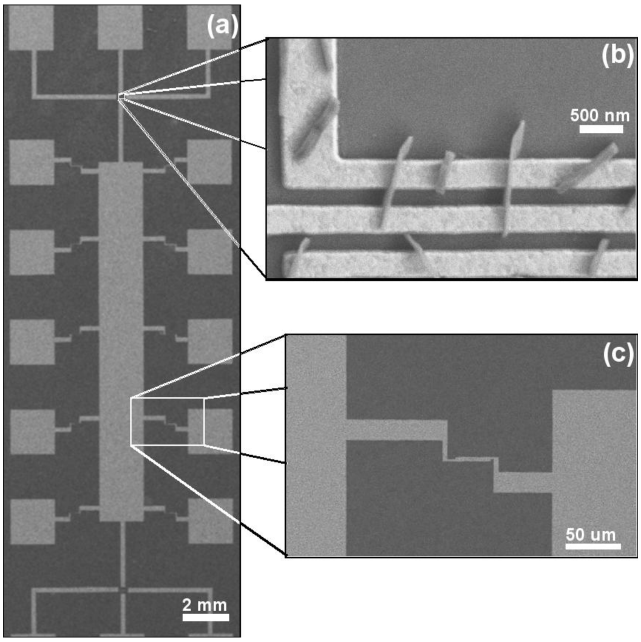

Figure 59: SEM images of device platforms fabricated by NIL, after p6P deposition

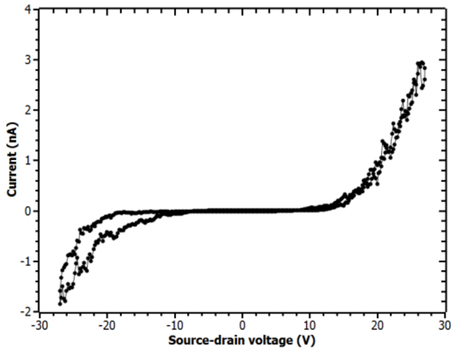

Figure 60: Electrical characterization for nanofiber devices fabricated by NIL.

6.8 CHAPTER SUMMARY

In this chapter, a method for large scale fabrication of device platforms for integrated nanofiber growth by nano-imprint lithography was presented. With this technique, both micro- and nano-scaled metal structures are fabricated in a single imprint step on a wafer scale.

The nano-imprint process was optimized from mold fabrication, stamp fabrication and anti-sticking coating to imprint, metal deposition and lift-off. The process optimization is not trivial, but once the recipe is working, it is quite reproducible.

Additional device platforms were fabricated with the tool *Imprio 100*, in collaboration with our partners from the Innovation consortium Octopus.

Production of device platforms on a large scale makes it possible to produce devices at large scale, since the nanofiber growth can be performed at large scale, by evaporating the p6P molecules on the heated substrate.

CHAPTER 7

CONCLUSIONS AND OUTLOOK

When p6P molecules are deposited on heated muscovite mica substrates, long and mutually parallel nanofibers are formed on the substrate surface. As mica is not further processable, it is not suitable as a device platform. Due to well-developed processing technology for silicon, this one constitutes a better device platform. Therefore, an alternative growth substrate consists of gold films deposited on silicon. Upon deposition of p6P molecules on gold surfaces, nanofibers are formed, but without the alignment observed for the nanofibers grown on mica. It has previously been shown [45] that the nanofibers grown on gold films containing micro-ridges can have their growth direction controlled by the micro-structures.

In this Ph.D. project, a method for controlling orientation, length and position of p6P nanofibers on gold was demonstrated. Nano-scaled titanium pinning lines were fabricated by e-beam lithography, metal deposition and lift-off on gold films deposited on silicon. Deposition of p6P molecules on these substrates leads to nanofiber growth. Under optimum growth conditions, the nanofibers are grown perpendicular to the pinning lines (orientation control) and bridging two successive lines, which means that the distance between two lines is determining the nanofiber length (length control). In addition, we have shown that by inserting small nucleation structures along the pinning line long axis, the growth position can be controlled, since the nanofibers tend to grow from such nucleation structures (position control).

An investigation of nanofiber growth on grating structures is also presented. We have found that it is possible to obtain p6P nanostructures both on titanium gratings on gold and on gold gratings on silicon dioxide. The resulting structures grow on the metal lines, usually across them, enabling the fabrication of device platforms where the gold electrodes and the organic structures are already isolated from the silicon substrate, with electrical connection to the gold electrodes. Electrical characterization of the devices containing p6P nanostructures grown on gold gratings on silicon dioxide was performed and the results were compared to a device containing a single transferred fiber. Much higher average current densities was found in the single fiber case, presumably due to the fact that not all the directed grown fibers have good electrical contact to the gold electrodes. Therefore, the device platforms were re-designed to a configuration containing only a single pair of gold electrodes separated by a small gap. The fibers grow on the gold electrodes and bridge the gap, thereby establishing electrical contact.

Three device platforms were implemented for in-situ directed growth of p6P nanostructures. The first of them consisted of platforms for organic field effect transistors. Two gold electrodes are fabricated on silicon dioxide and act as source and drain electrodes in a transistor platform. The morphology of the grown nanofibers is strongly influenced by the drain and source electrodes´ width. When the gold electrodes are narrow, the p6P molecules form high and narrow flake-like structures. This could be explained by topographic boundaries for p6P diffusion on these substrates, which leads to more vertical aggregation. On wider gold electrodes, the larger surface diffusion areas lead to nanofiber growth, similar to the fibers grown on plane gold surfaces. The turn-on voltage for the nanofibers is lower than for the nanoflakes. This could be due to the fact that the nanofibers have a larger contact area with the electrodes, which reduces the contact resistance. Both kinds of structures present typical electrical characteristics of an organic semiconductor connected to a metal electrode causing an injection barrier, and leading the current to start flowing after application of a certain voltage. The output curves do not present saturation, and this can be attributed to short-channel effects, since our channel (gap between the gold electrodes) is limited to 200 nm, which is the maximum gap for having bridging nanostructures. The curves also present hysteresis, which can be attributed to mobile charges inserted on the silicon dioxide during device fabrication.

Two different transistor configurations were characterized. The first consists of a bottom-gate configuration, where the highly doped underlying silicon is the gate electrode and the gate dielectric is the silicon dioxide, which is located closer to the substrate than the source and drain electrodes and the semiconductor. In the second configuration (top-gate), the gate dielectric is PMMA, which is deposited on top of the source and drain electrodes and the organic semiconductor. In both configurations, the conductivity is increased when a negative voltage is applied to the gate, confirming that holes are the primary charge carriers. However, the top-gate configuration results in a larger gate effect. This can be attributed to the larger contact area from which carriers inject.

Additionally, we have demonstrated a method to determine the intrinsic electrical properties of p6P nanostructures, in-situ grown on gold electrodes. This method consists of growing the organic structures across four individually connected gold lines, allowing 4-probe measurements to be performed. The values for the materials resistivity are dependent on the nanostructures degree of crystallinity. The resistivity of an amorphous p6P thin film is about 30450 Ω.m, while the average resistivity value for crystalline nanostructures is about 470 Ω.m, which is 65 times lower than the thin film resistivity.

Finally, platforms for light-emitting devices were implemented. It consists of bottom-gate transistors, where the source and drain electrodes are formed as a gold grating with the lines connected to two electrodes. This configuration enables a larger number of in-situ grown fibers, which facilitates the light detection. When an AC voltage is applied to the gate (drain and source symmetrically biased), both holes and electrons are injected into the p6P nanostructures. When these holes and electrons recombine, the nanostructures emit light. Parameters such as the amplitude and frequency of the AC gate voltage and the source and drain voltage have an influence on the emitted light intensity.

A method for large-scale fabrication of the device platforms by nano-imprint lithography was developed. Both micro- and nano-scaled structures can be fabricated on a wafer scale in a single imprint step, preventing the time consumpting e-beam lithography plus photolithography steps.

In conclusion, this project shows how large-scale fabrication of organic nanofiber based devices can be performed by in-situ grown of the nanofibers on the device platforms. Different nanostructures morphologies can be tailored by changing the growth substrate design, as illustrated in Figure 61.

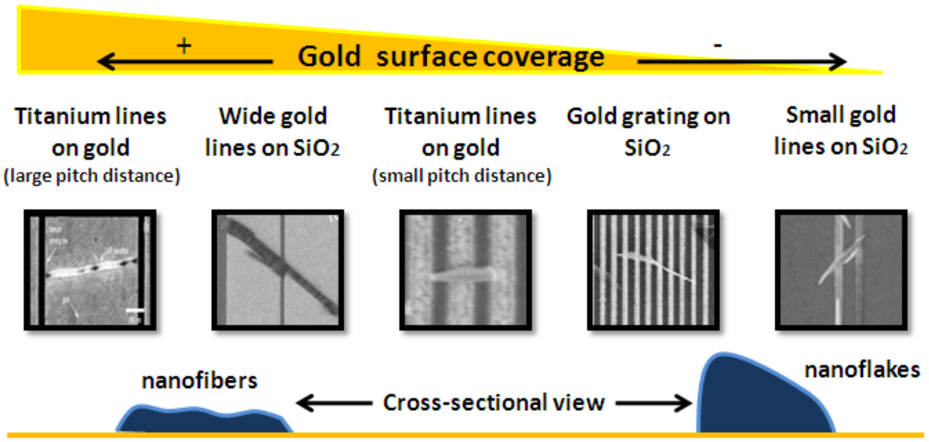

Figure 61: Nanostructures morphology dependence on the growth substrate design.

Future work should focus on molecular modification, since the electrical and optoelectronic properties of the organic nanofibers can be tailored by changing the molecular building-blocks. In addition, devices containing titanium pinning lines (and nucleation points) isolated from the gold layer should be developed and implemented (see attachment 1).

In order to improve the characteristics for the OFETs devices, short-channel effects should be avoided. This could be achieved by changing the gate dielectric thickness, and eventually the dielectric material. Also, the fabrication steps which introduce charges into the silicon dioxide (plasma asher and e-beam lithography) should also be avoided, preventing device hysteresis. The plasma asher is used for removing any organic residues before p6P deposition. An option to this process is to use chemicals to clean the sample before the nanofiber growth. The e-beam lithography can be exchanged with nanoimprint lithography, as was shown before.

We have observed a stronger gate effect for the OFETs for the top-gate configuration. Therefore, the light intensity emitted from light-emitting devices can be increased if the device is designed with a top-gate configuration. However, it requires a transparent metal electrode, so that the light can be detected. A device with such a configuration should be implemented in future work.

REFERENCES

[1] Monat, C.; Domachuk, P.; Eggleton, B. J.; *Nat. Photonics* 1**,** 106 (2007)

[2] Agarwal, R.; Lieber, C. M.; *Appl. Phys. A: Mater. Sci. Process*. 85, 209 (2006)

[3] Lai, E.; Kim, W.; Yang, P.; *Nano Res*. 1, 123 (2008)

[4] Duan, X.; Huang, Y.; Agarwal, R.; Lieber, C. M.; *Nature* 421, 241 (2003)

[5] Fan, Z.; Ho, J. C.; Jacobson, Z. A.; Razavi, H.; Javey, A.; *Proc. Natl. Acad. Sci. U.S.A.* 105, 11066 (2008)

[6] Sirbuly, D. J. *et. al.*; *Proc. Natl. Acad. Sci. U.S.A.* 102, 7800 (2005)

[7] Sirbuly D. J.; Tao, A.; Law, M.; Fan, R.; Yang, P.; *Adv. Mater.* 19, 61 (2007)

[8] Minot, E. D. *et. al.; Nano Lett*. 7 (2), 367 (2007)

[9] Law, J. B. K.; Thong, J. T.L.; *Appl. Phys. Lett*. 88, 133114 (2006)

[10] Fan, Z. *et. al.; Nano Lett.* 8 (1), 20 (2008)

[11] Svensson, C.P.T. *et al; Nanotechnology* 19, 305201(2008)

[12] Müllen, K.; Scherf, U. *Organic Ligth Emitting Devices* (Wiley-VCH Weinheim-2005)

[13] Hoppe, H.; Sariciftci, N.S.; *J. Mater. Res.* 19, 1924 (2004)

[14] Lim, S.J.; An, B.K.; Jung, S.D.; Chung, M.A.; Park, S.Y.; *Angew. Chem., Int. Ed.* 43, 6346 (2004)

[15] Huang, Y.; Duan, X.; Wei, Q.; Lieber, C. M.; *Science* 291, 630 (2001)

[16] Mårtensson, T.; Borgström, M.; Seifert, W.; Ohlsson, B. J.; Samuelson, L.; *Nanotechnology* 14, 1255 (2003)

[17] Mårtensson, T. *et al.*; *Nano Lett.* 4, 1987 (2004)

[18] Svensson, C.P.T. *et al.*; *Nanotechnology*, 19, 305201/1-305201/6 (2008)

[19] Balzer, F.; Rubahn, H.-G.; *Appl. Phys. Lett.* 79, 3860 (2001)

[20] Schiek, M.; Balzer, F.; Al-Shamery, K.; Brewer, J. R.; Lützen, A.; Rubahn, H.-G.; *Small* 4, 176 (2008)

[21] Schiek, M.; Lützen, A.; Koch, R.; Al-Shamery, K.; Balzer, F.; Frese, R.; Rubahn, H.-G.; *Appl. Phys. Lett.* 86, 153107/1-153107/3 (2005)

[22] Balzer, F.; Bordo, V. G.; Simonsen, A.C.; Rubahn, H.-G.; *Phys. Rev. B* 67, 115408/1-115408/8 (2003)

[23] Quochi, F.; Cordella, F.; Mura, A.; Bongiovanni, G.; Balzer, F.; Rubahn, H.-G.; *J. Phys. Chem. B* 109, 21690-21693 (2005)

[24] Kjelstrup-Hansen, J.; Henrichsen, H. H.; Bøggild, P.; Rubahn, H.-G.; *Thin Solid Films* 515, 827 (2006)

[25] Brewer, J.; Schiek, M.; Lützen, A.; Al-Shamery, K.; Rubahn, H.-G.; *Nano Lett.* 6, 2656 (2006)

[26] Kjelstrup-Hansen, J.; Hansen, O.; Rubahn, H.-G.; Bøggild, P.; *Small* 2, 660 (2006)

[27] Balzer, F.; Kankate, L.; Niehus, H.; Frese, R.; Maibohm, C.; Rubahn, H.-G.; *Nanotechnology* 17, 984 (2006)

[28] Madsen, M.; Kjelstrup-Hansen, J; Rubahn, H-G.; *Nanotechnology* 20, 115601/1-115601/5 (2009)

[29] Stampfl, J.; Tasch, S.; Leising, G.; Scherf, U.; *Synth. Met.* 71, 2125 (1995)

[30] Baker, K. N.; Fratini, A. V.; Resch, T.; Knachel, H. C.; Adams, W. W.; Socci, E. P.; Farmer, B. L.; *Polymer* 34 (8), 1571 (1993)

[31] Yanagi, H.; Okamoto, S.; *Appl. Phys. Lett.* 71, 2563 (1997)

[32] Resel, R.; Leising, G.; *Surface Science*, 409, 302 (1998)

[33] Resel, R.; Koch, N.; Meghdadi, F.; Leising, G.; Unzog, W.; Reichman, K.; *Thin Solid Films* 305, 232 (1997)

[34] Erlacher, K. *et al.; Surf. Sci.* 437, 191 (1999)

[35] Müller, B.; Kuhlmann, T.; Lischka, K.; Schwer, H.; Resel, R.; Leising, G.; *Surf. Sci.* 418, 256 (1998)

[36] Andreev, A.; Matt, G.; Brabec, C. J.; Sitter, H.; Badt, D.; Seyringer, H.; Sariciftci, N.S.; *Adv. Mat.* 12, 629 (2000)

[37] Plank, H.; Resel, R.; Purger, S.; Keckes, K.; Thierry, A.; Lotz, B.; Andreev, A.; Sariciftci, N.S.; Sitter, H.; *Physical Review B* 64, 235423 (2001)

[38] Miyake, S.; *Appl. Phys. Lett.* 65 (8) (1994)

[39] Griffen, D.; *Silicate Crystal Chemistry* (New York: Oxford University Press-1992)

[40] Madsen, M.; Ph.D thesis, University of Southern Denmark (2009)

[41] Thilsing-Hansen, K. Ph.D. thesis, University of Southern Denmark (2010)

[42] Odelius, M.; Bernasconi, M.; Parinello, M.; *Phys. Rev. Lett.* 78, 2855 (1997)

[43] Porter, D.; Easterling, K.; *Phase transformations in Metals and Alloys* (Boca Raton, FL: CRC Press) ISBN: 0-7487-5741-4

[44] Madsen, M; Kartopu, G.; Andersen, N.L.; Es-souni, M.; Rubahn, H..-G.; *Appl. Phys. A* 96, 591-594 (2009)

[45] Madsen, M.; Kjelstrup-Hansen,J.; Rubahn,H.-G.; *Nanotechnology* 20, 115601/1-5 (2009)

[46] Madsen, M.; Hansen, R.M. de O.; Kjelstrup-Hansen, J.; Rubahn, H.-G.; *Proceedings of SPIE*, 7406, 7406R-1 (2009)

[47] Kankate, L., Balzer, F., Niehus, H.; Rubahn, H.-G.; *J. Chem. Phys.* 128, 084709 (2008)

[48] Hansen, R.M. de O.; Kjelstrup-Hansen, J.; Rubahn, H.-G.; *Nanoscale*, 2, 134 (2010)

[49] Hansen, R.M. de O.; Madsen, M.; Kjelstrup-Hansen, J.; Pedersen, R. H.; Gadegaard, N.; Rubahn, H.-G.; *Proc. of SPIE* 7764 77640L-1(2010)

[50] Henrichsen, H. H.; Kjelstrup-Hansen, J.; Engstrøm, D.; Clausen, C. H.; Bøggild, P.; Rubahn, H-G.; *Organ. Electron*. 8, 540-544 (2007)

[51] de Boer, R. W. I.; Jochemsen, M.; Klapwijk, T. M.; Morpugo, A. F.; Niemax, J.; Tripathi, A. K.; Pflaum, J.; *J. Appl. Phys*. 95, 1196 (2004)

[52] Lampert, M. A.; Mark, P. *Current Injection in Solids*, (Academic Press, New York-1970).

[53] Zaumseil, J.; Sirringhaus, H.; *Chem. Rev.* 107, 1296-1323 (2007)

[54] Michaelson, H.B.; *Journal of Applied Physics,* 48, 11, 4729 (1977)

[55] Hansen, R.M. de O.; Madsen, M.; Kjelstrup-Hansen, J.; Rubahn, H.-G.; *Nanoscale Research Letters*, 6, 11 (2011)

[56] Chua, L.L.; Ho, P.K.H.; Sirringhaus, H.; Friend, R.H.; *Appl. Phys. Lett.* 84, 3400 (2004)

[57] Frank, D. J.; Dennard, R. H.; Nowak, E.; Solomon, P. M.; Taur, Y.; Wong, H. S. P.; *Proc. IEEE* 89, 259 (2001)

[58*] IEEE standard for test methods for the characterization of organic transistors and materials* (2008)

[59] Jung, T.; Dodabalapur, A.; Wenz, R.; Mahapatra, S.; *Appl. Phys. Lett.* 87, 182109 (2005)

[60] Tavares, L.; Kjelstrup-Hansen, J.; Thilsing-Hansen, K.; Rubahn, H.-G.; Accepted for publication at *Nanoscale Research Letters* (2011)

[61] Hill, I. G.; *Appl. Phys. Lett*. 87, 163505 (2005)

[62] Das, A. *et al*.; *Nature Nanotech*., 3, 210 (2008)

[63] Klauk, H. *et al*.; *J. Appl. Phys*, 92, 5259 (2002)

[64] Plummer, J. D.; Deal, M. D.; Griffin, P.B.; *Silicon VLSI Technology* (Prentice Hall-2000)

[65] Egginger, M.; Bauer, S.; Schwodiauer, R.; Neugebauer, H.; Sariciftci, N.S.; *Monatsh. Chem.* 140, 735-750 (2009)

[66] Mathijssen, S.G.J. *et al*.; *Adv. Mater*. 20, 975 (2008)

[67] Sirringhaus, H. *et al*.; Science, 290, 2123 (2000)

[68] Austin, M. D.; Chou, S. Y.; *Appl. Phys. Lett*. 81, 4431 (2002)

[69] Sequeira, C.A.C; Santos D.M.F.; *Brazilian Journal of Physics*, 37, 3B, 1077 (2007)

[70] Anthony, J.E.; Brooks, J.; Eaton, D.L.; Parkin, S., *J. Am. Chem. Soc.*, 123, 9482 (2001)

[71] Kjelstrup-Hansen, J.; Liu, X.; Henrichsen, H. H.; Thilsing-Hansen, K.; Rubahn, H.-G.; *Phys. Status Solidi C*, 1-4 (2010)

[72] Liu, X.; Wallmann, I.; Boudinov, H.; Kjelstrup-Hansen, J.; Schiek, M.; Lutzen, A.; Rubahn, H.-G.; *Organic electronics* 11 1096-1102 (2010)

[73] Chou, S.Y.; Krauss, P.R.; Renstrom, P. J.; *Applied Physics Letters* 67, 3114 (1995)

[74] Beck, M.; Graczyk, M.; Maximov, I.; Sarwe, E.-L.; Ling, T.G.I.; Keil, M.; Montelius, L.; *Microelectronic Engineering* 61-62, 441-448 (2002)

[75] NIL Library of processes:
http://www.napanil.org/index.php?page=publications

[76] Bender, M. *et al.*; *Microelectronics Engineering*, 61-62, 407-413 (2002)

[77] Rampi, M. A.; Schueller, O. J. A.; Whitesides, G. M.; *Appl. Phys. Lett. 72*, 1781-1783 (1998)

[78] Ulman, A.; *Chem. Rev*. 96, 1533-1554 (1996)

[79] Zhang, L.; Zhong, J.; Huang, L.; Wang, L.; Hong, Y. and Sha, Y.; *J. Phys. Chem. B, 112,* 8950–8954 (2008)

LIST OF PUBLICATIONS

The publications related to this Ph.D. project are listed below:

Peer-review Papers:

"Pinning of organic nanofiber surface growth"
Nanoscale, 2, 134-138, 2010
Authors: Roana Melina de Oliveira Hansen, Jakob Kjelstrup-Hansen and Horst-Günter Rubahn

"In situ-directed growth of organic nanofibers and nanoflakes: electrical and morphological properties"
Nanoscale Research Letters, 6, 11, 2011
Authors: Roana Melina de Oliveira Hansen, Morten Madsen, Jakob Kjelstrup-Hansen and Horst- Günter Rubahn

"*Optical properties of microstructured surface-grown and transferred organic nanofibers"*
Accepted for publication at Journal of Nanophotonics, 2011
Authors: Jakob Kjelstrup-Hansen, Luciana Tavares, Roana Melina de Oliveira Hansen, Xuhai Liu, Kirill Bordo and Horst-Günter Rubahn

"In-situ growth of organic nanofibers on top-gate transistor and 4-point measurements platforms"
In preparation
Authors: Roana Melina de Oliveira Hansen, Luciana Tavares, Jakob Kjelstrup-Hansen and Horst-Günter Rubahn

Proceedings:

"Controlled growth of organic nanofibers on nano- and micro-structured gold surfaces"
Proceedings of SPIE, 7406, 7406R-1, 2009
Authors: Morten Madsen, Roana Melina de Oliveira Hansen, Jakob Kjelstrup-Hansen and Horst- Günter Rubahn

"Electrical properties of in-situ grown and transferred organic nanofibers"
Proceedings of SPIE, 7764, 77640L-8, 2010
Authors: Roana Melina de Oliveira Hansen, Morten Madsen, Jakob Kjelstrup-Hansen, Rasmus Haugstrup Pedersen, Nikolaj Gadegaard and Horst-Günter Rubahn

Posters and talks at conferences:

“Surface Structure Directed Growth of Nanomaterials”
Published abstract at “2nd German-Danish meeting on interface related phenomena”, 2008
Authors: Roana Melina de Oliveira, Morten Madsen, Jakob Kjelstrup-Hansen and Horst-Günter Rubahn

“Templates Patterned by e-beam Lithography for Integrated Nanofiber Growth”
Poster presentation at ”Third Summer School of the European Doctorate in Physics and Chemistry of Advanced Materials”, Lithuania, 2008
Authors: Roana Melina de Oliveira, Morten Madsen, Jakob Kjelstrup-Hansen and Horst-Günter Rubahn

“Growth of oriented organic nanofibers on micro-structured gold surfaces”
Published abstract at “Nanotech Northern Europe”, Copenhagen, Denmark, 2008
Authors: Morten Madsen, Roana Melina de Oliveira, Jakob Kjelstrup-Hansen and Horst-Günter Rubahn

“Organic Nanofiber Surface Growth Control”
Poster presentation at ”Annual Meeting for The Danish Optical Society (DOPS), 2009
Authors: Roana Melina de Oliveira Hansen, Jakob Kjelstrup-Hansen and Horst-Günter Rubahn

“Organic Nanofiber Surface Growth Control”
Poster presentation at ” Smart Materials and Structures”, Kiev, Germany, 2009
Authors: Roana Melina de Oliveira Hansen, Jakob Kjelstrup-Hansen and Horst-Günter Rubahn

“Templates for integrated nanofiber growth”
Poster presentation at ICPEPA-7, Copenhagen, Denmark, 2010
Authors: Roana Melina de Oliveira Hansen, Jakob Kjelstrup-Hansen and Horst-Günter Rubahn

ATTACHMENT 1: AN OUTLOOK FOR FUTURE WORK

In chapter 3, a method for achieving growth control of length and orientation of p6P nanofibers by growing them between titanium pinning lines was demonstrated. A further development of this method was performed, where nano-scaled nucleation points were inserted on the pinning lines in order to achieve position control, as shown in chapter 3. By taking use of this method, the nanofibers could be grown in specific sites on the device, which would be very useful for many different applications [49]. However, to grow the nanofibers on a gold film containing titanium pinning lines is not sufficient to develop practical devices, since the titanium lines (electrodes) are connected to the gold film, as well the grown nanofibers, which does not allow electrical characterization.

Self-assembled monolayers (SAMs) are composed by organized layers of molecules in which one end of the molecule shows a special affinity for the substrate, as shown on Figure 62. They can for example be deposited by immersing the substrate on a dilute solution of the molecule at ambient conditions for a couple of hours. Some monolayers present electrical insulating properties [77] and at the same time are thin enough to allow the nanofiber formation if deposited on a gold film [78-79].

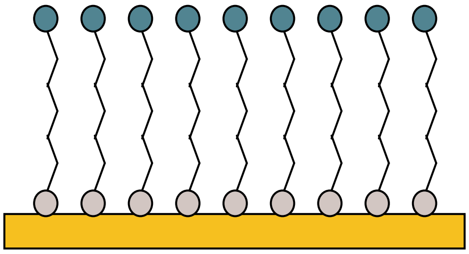

Figure 62: Schema showing a self-assembled monolayer of molecules on a gold substrate.

SAMs deposited on gold films are an option for an insulating layer. If the p6P nanofibers could be formed on this layer, they could be grown electrically isolated from the gold substrate.

The next step was to define a way to isolate the titanium pinning lines, which would act as electrodes, from the gold layer. One possibility is to have a layer of silicon nitride under the titanium lines, as shown in Figure 63. In this way, the electrodes will be isolated from the bulk substrate.

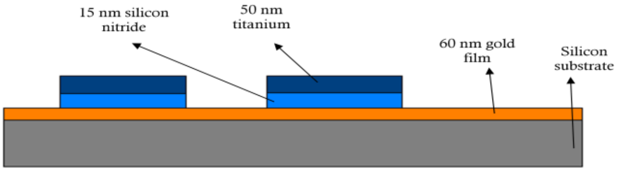

Figure 63: Cross-section of a substrate where the titanium pinning lines are isolated from the gold substrate.

Some attempts for fabricating such a device were made, by first depositing a 15 nm silicon nitride layer (PECVD) on top of the sputtered gold layer and then patterning the titanium pinning lines by e-beam lithography, titanium deposition and lift-off. The silicon nitride was then etched (dry plasma etching using a mixture of $SF_6/O_2/N_2$) all the way until the gold layer, using the titanium structures as etching mask. The fabricated pinning lines are connected to large titanium pads, which facilitates electrical connection.

A self-assembled monolayer of octadecanethiol was formed on this substrate by immersing the sample in a solution (octadecanethiol dissolved in pure ethanol to form 1.0×10^{-3} M solution) for about 12 hours. However, the SAM quality was not characterized. Afterwards, p6P molecules were deposited by vapor deposition of p6P molecules (thickness of 5 nm) onto heated substrates (175°C) under high vacuum conditions (~ 10^{-8} mbar). The nominal thickness and deposition rate (~ 0.1 Å/s) was monitored by a water-cooled quartz microbalance.

Figure 64 is an SEM image of the Ti/silicon nitride structures on gold. After p6P deposition, the resulting nanofibers are perpendicular to the pinning lines, as can be seen in Figure 65. The dashed lines are a guide to the eye showing the titanium/gold edges.

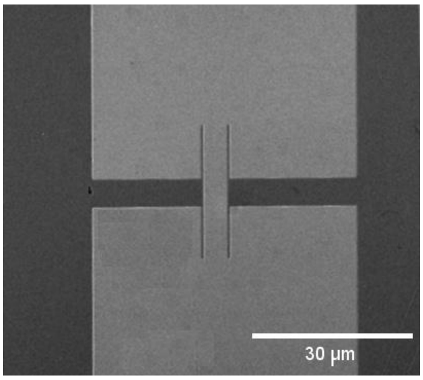

Figure 64: SEM image of the titanium/silicon nitride structures on gold.

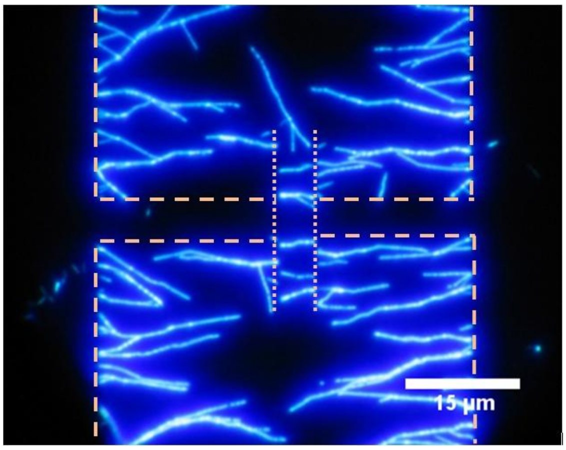

Figure 65: Fluorescence microscopy image of the nanofibers grown on the described substrate.

These results suggest that it is possible to design a substrate where both the nanofibers and electrodes are isolated from the gold film. However, electrical tests were made on these samples before p6P deposition, and electrical short-circuits were observed. This can be due either the thin silicon nitride layer thickness (or quality) or damaging of electrodes during wire bonding. Also, the SAM should be better characterized, in order to determine its properties.

Further development of this design substrate including structured pinning lines with nucleation points is very promising for different applications and should be considered as an outlook.

ATTACHMENT 2: NIL PROCESS

SILICON MOLD PREPARATION:

1. Wafer cleaning.
    1. Soak in Piranha solution for 10 minutes
    2. Soak in DI water for 1 minute
    3. Spin dry
2. Photolithography.
    1. HMDS oven for 30 minutes
    2. Spin on photo resist AZ 5214E (500 RPM for 5 s, 4000 RPM for 30 s), prebake at 90°C for 60 s
    3. Exposure (2.1 s, soft contact)
    4. Inversion bake (130° C for 120 s)
    5. Flood exposure (30 s)
    6. Development (AZ 351B, 22°C, 60 s, rinse in water for 2 min, spin dry)
    7. Etch silicon in ICP-RIE (recipe: PMMA mask, for 4.5 s)
    8. Remove resist: Acetone wet bench, rinse in water, spin dry
3. Wafer cleaning.
    1. Plasma asher (5 minutes, 200 W)
4. EBL.
    1. PMMA A4, 4000 RPM, 45 s
    2. Pre-bake, 200°C for 90 s
    3. E-beam lithography (area dose= 350)
    4. Development (1:3 MIBK:IPA, 40 s, rinse in IPA for 30 s)
    5. Etch silicon in ICP-RIE (recipe: PMMA mask, for 5.5 s)
    6. Remove PMMA: Acetone wet bench, rinse in water, spin dry
5. Anti-stick layer.
    1. Plasma asher (5 minutes, 200 W)
    2. Prepare a solution of 0.5% surfactant (1 ml F_{13}-TCS to 200 ml heptane)
    3. Immerse the wafer in the solution for 3 hours
    4. Rinse the wafer using heptane
    5. Blow dry N_2
    6. Bake the wafer at 180°C for 2 minutes

QUICKMOLD STAMP FABRICATION:

1. Plate cleaning.
    1. Soak in Piranha solution for 10 minutes
    2. Soak in DI water for 1 minute
    3. Blow dry
2. QuickMold polymer
    1. Spin-coat plate with AR-ULP at 4000 RPM for 45 seconds
    2. Bake on hotplate at 200°C for 120 seconds.
    3. Spin-coat plate with AR-UVM at 2000 RPM for 7 seconds
3. Imprint
    1. Imprint plate using Si master mold
    2. Pi=1 psi, Ps=20 psi, T1= 300 s, T2= 5 s, T3= 120 s.
    3. Cure at 8 mW/cm2 for 500 seconds (release wafer when 200 seconds are remaining)
4. Oxidize the surface: treat plate on plasma asher, 80W, 10 s.
5. Anti-stick layer.
    1. Prepare a solution of 0.5% surfactant (1 ml F_{13}-TCS to 200 ml heptane)
    2. Immerse the plate in the solution for 60 minutes
    3. Rinse the plate using heptane
    4. Blow dry N_2
    5. Bake the plate at 180°C for 2 minutes

IMPRINT PROCESS:

1. Wafer cleaning.
    1. Soak in Piranha solution for 10 minutes
    2. Soak in DI water for 1 minute
    3. Spin dry
2. Apply polymer.
    1. Spin-coat wafer with AR-ULP at 4000 RPM for 45 seconds
    2. Bake on hotplate at 200°C for 90 seconds.
    3. Spin-coat wafer with AP-UV at 5000 RPM for 7 seconds
3. Imprint.
    1. Imprint wafer using QuickMold stamp
    2. Pi: 1 psi, Ps=28 psi, T1= 120 s, T2= 2 s, T3= 60 s.
    3. Check for leaks (vacuum must be between 700 and 760 mmHg)
    4. Cure at 8 mW/cm2 for 250 s

POLYMER FILM ETCH:

1. Etch AR-UV residual layer
    1. Gas flow: 3 sccm O2 + 15 sccm SF6
    2. Power: 80 W (chuck: 40 W)
    3. Time: 1 minute
2. Etch AR-UL underlayer
    1. Gas flow: 25 sccm O2
    2. Power 80 W (chuck: 50 W)
    3. Time: 3 minutes

METAL DEPOSITION:

1. Deposit 2 nm Ti + 30 nm Au by e-beam evaporation

LIFT-OFF:

1. Acetone wet bench, 5 minutes of sonication
2. Rinse with DI
3. Spin dry